

III. CONFINEMENT

R. J. GOLDSTON (PPPL), R. E. WALTZ (GA) G. BATEMAN (PPPL), D. P. STOTLER (PPPL),
C. E. SINGER, and J. KINSEY (University of Illinois)

The problem of projecting the energy confinement properties of future devices is a long-standing one in toroidal confinement research. While substantial progress has been made in characterizing the transport properties of tokamaks and stellarators, no definitive understanding of the mechanism(s) of cross-field transport has been achieved. Thus, we are not in a position to perform "first-principles" calculations of the projected performance of BPX. On the other hand, a wide range of data has been accumulated from tokamak experiments covering a large space of experimental parameters. These data have been used to constrain (or "calibrate") theory-based models and have also been fit with statistical regression models of varying degrees of sophistication, in order to perform projections to future devices. The BPX physics group, in collaboration with the Transport Task Force and the Doublet III-D (DIII-D) and Tokamak Fusion Test Reactor (TFTR) experimental teams, has recently begun to explore another avenue of approach, in which dimensionally scaled confinement (e.g., confinement time normalized by gyrofrequency $\Omega_c\tau_E$) is expressed in terms of key dimensionless variables such as β , collisionality ν_* , and gyroradius divided by plasma half-width ρ/a . BPX-like values of β and ν_* can be achieved in present devices, so the problem of projecting BPX performance can be reduced to the simpler one of determining the variation of $\Omega_c\tau_E$ with ρ/a . Theoretical models suggest that this variation should be particularly simple, e.g., quadratic or cubic.

This chapter presents the full range of different approaches to projecting the confinement performance of BPX. Section III.A presents a progress report on the dimensional scaling approach. Section III.B presents the status of theory-based simulations, calibrated against present data. Section III.C describes the history and status of empirically derived scaling relations and their projections for BPX. At the present time, it is this approach on which we rely most heavily to project the performance of BPX. Since the uncertainty in confinement projection is also a key issue, this section addresses the uncertainties in the key parameters affecting the overall fusion performance of BPX. Section III.D applies the results of Sec. III.C in order to determine the range of performance expected in BPX, on the basis of fixed-profile, steady-state, and time-dependent global transport modeling.

There is a substantial range of uncertainty associated with projecting from present experiments to high- Q devices such as BPX. Further results from present devices can be expected to narrow this range of uncertainty somewhat in the next few years. The development of better understanding and operational techniques may also improve the projected performance. An important element of the mission of BPX itself, however, is to investigate confinement in the high-performance alpha-heated regime, in order to develop techniques to optimize such plasmas for an Engineering Test Reactor, and in order to contribute to definitive scaling information for the design of a Demonstration Power Reactor.

III.A. THEORY-BASED PROJECTIONS OF BPX CONFINEMENT PERFORMANCE

R. E. Waltz (GA)

The mission of BPX is to study the physics of burning plasmas with the alpha power deposition supplying at least half the plasma heating. This sets $Q = 5$ as a minimum performance level, with a reasonable expectation of ignited or nearly ignited (high- Q) plasmas. Unlike most previous fusion devices, there is a required confinement performance without which the experimental objectives cannot be attained. The present BPX design is based on accepted empirical methods and models for describing and projecting tokamak confinement. Nevertheless, the BPX Physics Program is supporting ongoing work to establish physical or theoretical principles for projecting the confinement performance. In the near term, these principles will be based largely on dimensional analysis. Here we describe this ongoing work, comparing and contrasting our present theoretical understanding with the empirical models. At present, these physical principles can only supplement or bound the empirical projections. However, as we will show, where theoretical and empirical models differ, the existing theoretical models tend to project more optimistic performance.

III.A.1. Dimensional Analysis: Theory and Statistics

Tokamaks operate in a variety of confinement regimes: low-density neo-Alcator and high-density

saturated ohmic heating, L-mode high-power heating as well as H mode. This suggests that there may be several transport mechanisms at work. Even if these mechanisms were reasonably well understood, modeling them in sufficient detail to describe even the global confinement time would be very complex. However, we argue that our lack of complete understanding need not prevent us from accurately scaling present tokamaks to ignition devices of greater size (a) and magnetic field strength (B), provided we apply our most basic knowledge of the dimensional constraints on transport mechanisms.

The dimensionless parameters determining the scaling of diffusivity χ comprise a long but finite list. Those based on geometry are q , R/a , and b/a . Note that these fix $\beta_{crit} \propto a/Rq$. Those based on profiles are L_n/a , L_T/a , L_{shear}/a , and so forth. Finally, in addition to the atomic mass of the working gas A , Z_{eff} , and T_e/T_i , those based on pure plasma parameters are $\beta \propto nT/B^2$, collisionality $\nu_* \propto na/T^2$, and the relative gyroradius $\rho_* \propto T^{1/2}/Ba$, where $\rho_* \equiv \rho_s/a$ [$\rho_s = c_s/\Omega$, $c_s = (T/M)^{1/2}$, $\Omega = eB/Mc$]. Note that the relative Debye length is specifically excluded. There are many other dimensionless parameters, but they can be written in terms of this set. The confinement time τ is scaled by a^2/χ only if the relative heating profile parameter L_{heat}/a remains fixed. It is important to stress that atomic physics associated with the divertor and edge processes are assumed here to have a negligible effect on the overall confinement scaling. This is perhaps a questionable assumption, given the apparent importance of the edge in the transition to the H mode. Furthermore, new fast alpha-particle effects on confinement cannot be projected from these parameters. That is indeed why a Burning Plasma Experiment is needed.

Discharges with all these relevant dimensionless parameters held fixed could be called "dimensionally identical." It has been shown that dimensionally identical plasmas should have their global energy confinement time scaled to the gyrofrequency: $\tau \propto \Omega^{-1} \propto B^{-1}$ (Refs. 1 and 2). From this, the ignition parameter $nT\tau \propto \beta B^2 B^{-1} \propto B$. Along this dimensionally identical path, $n \propto B^{8/5}$, $T \propto B^{2/5}$, and $a \propto B^{-4/5}$. While it has been argued that all high- Q tokamaks will have almost the same dimensionless parameters as existing plasmas, it is not practical to scale existing discharges of largest $nT\tau$ to ignition with fully identical dimensionless parameters. However, it is possible to reach ignition parameters by scaling existing tokamak discharges with all dimensionless parameters fixed except the relative gyroradius ρ_* . We can call

these "dimensionally similar" discharges.

Theoretically, the scaling of dimensionally similar discharges with respect to relative gyroradius should be very simple. All existing theories fall at or near two extremes: those characterized by turbulence with short wavelengths scaled to intrinsic plasma parameters like the gyroradius (ρ_s) or the collisionless skin depth (c/ω_{pe}), which we call gyroBohm-like, and those with long wavelengths scaled to the plasma size (a), which we call Bohm-like. In the gyroBohm case, the diffusivity scales as $\chi_{gB} \propto (c_s/a)\rho_s^2 F_{gB}$, whereas for the Bohm case $\chi_B \propto c_s \rho_s F_B$. The F form factors represent the functional dependence on all the dimensionless parameters other than ρ_* , which are held fixed for dimensionally similar discharges. A survey of theoretical models in current use shows that nearly all are gyroBohm-like, and thus, their form factors may be simply added. For example, neoclassical diffusion, $E \times B$ drift wave diffusion, and stochastic magnetic field line transport from microtearing modes, or electromagnetic transport on the scale of the collisionless skin depth c/ω_{pe} , may all be rewritten in this form. An exception is a recent version of resistive magnetohydrodynamic (MHD) magnetic transport.³ In this case, numerical simulation of the turbulence suggests that the average poloidal wave number scales to q/a , giving an almost Bohm-like diffusion form $\chi \propto c_s \rho_s (\rho_s/a)^{1/3} F_{rmhd}$. For dimensionally similar discharges that must have density $n \propto B^{4/3} a^{-1/3}$, temperature $T \propto B^{2/3} a^{1/3}$, and $\rho_* \propto (B^4 a^5)^{-1/6}$ (for β and ν_* held constant), the diffusivity should scale as $\chi_{gB} \propto B^{-1} a^{-1/2}$ or $\chi_B \propto B^{-1/3} a^{1/3}$, at the extremes of gyroBohm or Bohm diffusion.

If experiments could verify that either the gyroBohm or Bohm extreme prevails, then we could have a powerful "wind tunnel"-like method for scaling fusion devices to high Q . If net heating profiles are self-similar, then the global confinement time should scale as $\tau \propto a^2/\chi$. For dimensionally similar discharges, we should expect $\tau_{gB} \propto \Omega^{-1} \rho_*^{-3} \propto B a^{5/2}$ or $\tau_B \propto \Omega^{-1} \rho_*^{-2} \propto B^{1/3} a^{5/3}$, which implies a substantial difference in the ignition parameter $nT\tau_{gB} \propto B^3 a^{5/2} \propto I^3/a^{1/2}$ or $nT\tau_B \propto B^{7/3} a^{5/3} \propto I^{7/3}/a^{2/3}$. While the preponderance of theoretical models have a gyroBohm-like scaling, the standard empirical L-mode scaling is somewhat worse than Bohm-like. For example, along a dimensionally similar path, the Goldston empirical scaling,⁴ which appears to give a good statistical characterization of the global confinement time based on diamagnetic stored energy, reduces to $\tau_{emp} \propto B^0 a^{1.8}$ with $nT\tau_{emp} \propto B^2 a^{1.8} \propto I^2/a^{0.2}$. Thus, in general, the theoretically based

models tend to give more optimistic projections to high Q .

The global confinement time τ can be statistically analyzed directly in terms of dimensionless parameter exponential forms

$$\tau \propto \Omega^{-1} \rho_*^{\alpha_1} [\nu_*^{\alpha_2} \beta^{\alpha_3} q^{\alpha_4} (R/a)^{\alpha_5} (b/a)^{\alpha_6} Z_{\text{eff}}^{\alpha_7} A^{\alpha_8}]$$

to determine the ρ_* exponent. When the diamagnetic stored energy is used to define τ , statistical analysis of the L-mode beam-heated data base shows that the exponent α_1 is worse than Bohm-like ($-2.0 < \alpha_1 < -1.5$), typical of Goldston's result. There have been recent attempts to "correct" the diamagnetic data base for fast ion stored energy^{5,6} and for neutral beam penetration effects.⁶ While these corrections redirect the scaling from Bohm-like toward gyroBohm-like ($\alpha_1 = 3$), they are very approximate and do nothing to address the uncertainties introduced by statistical covariations of the dimensionless parameters within the data base: roughly $\rho_* \propto \beta$ and $\nu_* \propto \beta^{-1}$. Furthermore, the ρ_* exponent α_1 is very sensitive to small changes in the machine variables fit:

$$\tau \propto B^{\alpha_B} P^{\alpha_P} n^{\alpha_n} a^{\alpha_a} [q^{\alpha_q} (b/a)^{\alpha_\kappa} (R/a)^{\alpha_\epsilon} A^{\alpha_A}].$$

We can show algebraically that for a dimensionally consistent fit,

$$\alpha_1 = -[9\alpha_P + 3\alpha_B + 4\alpha_n + 3]/[2\alpha_P + 2].$$

Note that α_1 determines the size scaling, and it can be determined without reference to the machine size exponent α_a . That illustrates the power of the dimensional constraint: Experiments in a single machine can in principle determine the tokamak size scaling. However, to illustrate the sensitivity, consider a few examples: For Goldston scaling [$\tau \propto I^{1.0} B^{0.0} P^{-0.5} n^{0.0} R^{1.75} a^{-0.37} (b/a)^{0.5} A^{0.5}$], $\alpha_B = 1.0$, $\alpha_P = -0.50$, and $\alpha_n = 0.0$, we have $\alpha_1 = -1.5$ (worse than Bohm-like). For ITER89-P L-mode scaling [$\tau \propto I^{0.85} B^{0.2} P^{-0.5} n^{0.1} R^{1.2} a^{0.3} (b/a)^{0.5} A^{0.5}$], $\alpha_B = 1.05$, $\alpha_P = -0.50$, and $\alpha_n = 0.1$, we have $\alpha_1 = -2.05$ (Bohm-like). For Kaye-Goldston [$\tau \propto I^{1.24} B^{-0.09} P^{-0.58} n^{0.26} R^{1.65} a^{-0.49} (b/a)^{0.5} A^{0.5}$], $\alpha_B = 1.15$, $\alpha_P = -0.58$, and $\alpha_n = 0.26$, we have $\alpha_1 = -2.7$ (almost gyroBohm-like). Note the high leverage of the density and power exponents. The correction for fast ion storage and beam penetration (not included in these fits) have the effect of increasing α_n and decreasing α_P .

Ohmic discharges in the "linear" neo-Alcator regime have a gyroBohm-like scaling. Along a dimensionally similar path, $\tau \propto n a R^2 q^{0.7} \propto B^{4/3}$. This is evidently closer to B than $B^{1/3}$. At fixed q ,

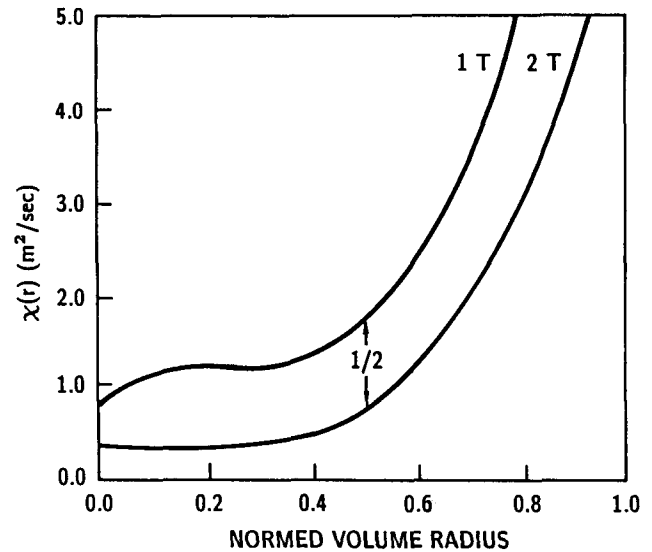


Fig. 3.1. DIII-D diffusivity comparing $B = 1$ T and $B = 2$ T dimensionally similar discharges. The relation $\chi \propto B^{-1}$ appears to be consistent with gyroBohm scaling.

the ohmic heating profile does not change with density. The mechanisms controlling L- and H-mode scaling are almost certainly different from those in the neo-Alcator regime (one could for example be gyroBohm-like and the other Bohm-like). Thus, while not a proof, it is a hint that the Bohm-like character of empirical L-mode scaling could be due to the parametric variability of neutral beam heating, which predominates in the currently available data base.

III.A.2. Dimensional Analysis: Controlled Experiments

To resolve the crucial ρ_* scaling, controlled experiments in DIII-D (Refs. 8 and 9) and TFTR (Ref. 9) comparing dimensionally similar discharges have been performed. These consisted of L-mode B scans at fixed q with $n \propto B^{4/3}$ and power adjusted to keep ν_* and β constant. This breaks the statistical covariance in the standard data base and allows a direct analysis of χ . Both experiments followed the Goldston empirical scaling with confinement time τ nearly constant in B . Both experiments had substantial variation of the beam deposition profile in scanning from low to high density. Unfortunately, these initial experiments appear to give contradictory results. As shown in Fig. 3.1, the DIII-D experiment clearly showed gyroBohm-like scaling for the diffusivity with $\chi \propto B^{-1}$. The failure of τ to scale linearly with B could be entirely accounted for by the poor beam penetration at the higher field and density. In contrast, the TFTR results shown in

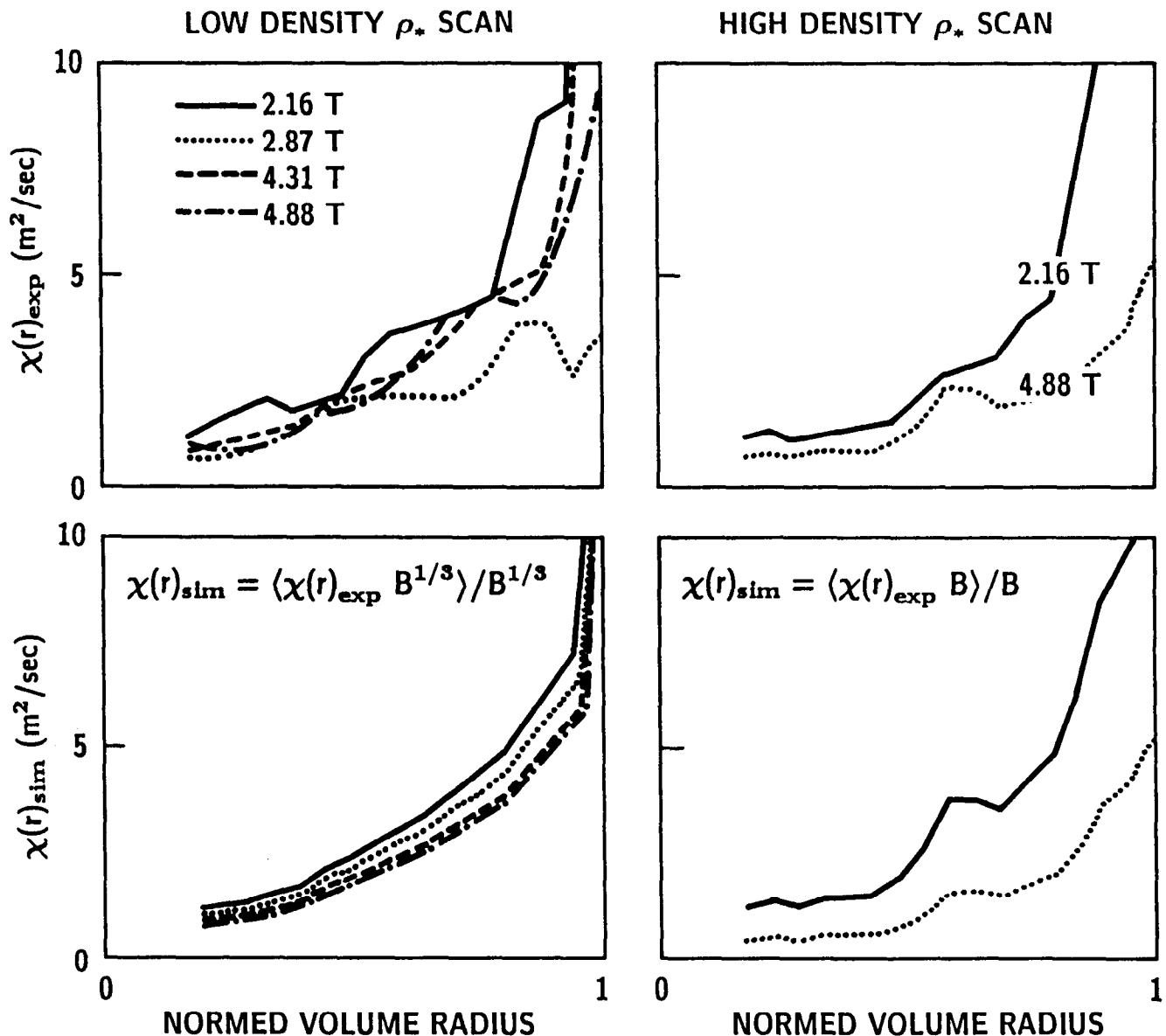


Fig. 3.2. TFTR diffusivities from dimensionally similar ρ_* scans at low and high density. The low-density scan appears to be most consistent with Bohm-like scaling ($\chi \propto B^{-1/3}$), although the high-density scan, which is more like the DIII-D experiment, appears to be gyroBohm-like.

Fig. 3.2 appeared to have a Bohm-like scaling with $\chi \propto B^{-1/3}$, although lack of temperature equilibration allowing T_e/T_i to vary made the similarity conditions difficult to satisfy and the experiment more difficult to analyze. Further attempts to make equilibrated discharges proved unsuccessful. More experiments on DIII-D are planned to repeat the ρ_* scan while maintaining heating profiles similarity by off-axis heating. The DIII-D and Joint European Torus (JET) teams plan to compare the profiles of dimensionally similar discharges to test the size scaling: $\chi_{gB} \propto B^{-1} a^{-1/2}$ or $\chi_B \propto B^{-1/3} a^{1/3}$.

In other experiments, density scans for nearly dimensionally identical ohmic discharges in Princeton Large Torus (PLT) and Alcator-C have been shown to overlay in $B\tau$ (Ref. 10). Discrepancies in overlays with TFTR ohmic scans appear to be due to rather extreme differences in the density profiles (L_n/a). Variations within TFTR show $B\tau$ invariant as expected. High-field, small inboard-limited discharges were compared with lower field outboard-limited discharges. Such experiments test the principles of dimensional analysis based solely on plasma physics. Also, initial ohmic ρ_* scans in TFTR appear to be consistent with

gyroBohm-like $\tau \propto B$ in the linear regime.

III.A.3. Dimensional Analysis: Projections to High Q

Projecting dimensionally similar discharges to ignition is quite straightforward. Although it is as yet unclear whether the underlying physics is gyroBohm-like or Bohm-like, it is reasonable to assume performance is bounded by these extremes in the absence of deleterious alpha-particle effects. A given experimental discharge with minor radius a and magnetic field B projects to a corresponding BPX discharge at $a = 0.79$ m and $B = 9$ T with the same β , collisionality ν_* , q , elongation b/a , and aspect ratio R/a . Since the BPX aspect ratio is fixed and may not be exactly the same as that in the experiment, we need a further empirical assumption on aspect ratio scaling. Recent TFTR aspect ratio experiments¹⁰ have shown that the ignition parameter is a function of $IR/a \propto Ba$ at fixed q and b/a , independent of large changes in the aspect ratio with B and a each held fixed. Thus, even changing the aspect ratio, the ignition parameter $n(0)T(0)\tau$ must be scaled by $B^{7/3}a^{5/3}$ for Bohm-like confinement or $B^3a^{5/2}$ for gyroBohm-like confinement as density and temperature are rescaled by $n(0) \propto B^{4/3}a^{-1/3}$ and $T(0) \propto B^{2/3}a^{1/3}$. From this it follows that the confinement times and sustaining power rescale as $\tau \propto B^{1/3}a^{5/3}$ or $Ba^{5/2}$ and $P \propto Ba^{1/2}(R/a)$ or $B^{5/3}a^{4/3}(R/a)$. [I rescales by $Ba(a/R)$.] The actual auxiliary power needed for the fusion plasma is given by $P_{aux} = P/[(Q/5) + 1]$. The Q is obtained by computing the fusion alpha power gain minus bremsstrahlung power loss at the rescaled density and temperature.

Table 3.1 illustrates this simple projection process for two high- $nT\tau$ H-mode deuterium shots from DIII-D and JET (Ref. 12). Care was taken to make dW/dt subtractions on the power data. $Z_{eff} = 1.5$ and a D-T depletion factor of 0.84 are assumed here, and no advantage of atomic mass over deuterium was taken. Figure 3.3 illustrates the projection of the ITER90 H-mode data base for DIII-D and JET on to the universal $n(0)T(0)\tau$ versus $T(0)Q$ -contours. The contours depend only on the profile shapes, which we have assumed to have parabolic exponents $\alpha_n = 0.5$ and $\alpha_T = 1.0$. The total stored energy and $\langle n \rangle$ were used to deduce $n(0)$ and $T(0)$. The special shots of Table 3.1 (not in the ITER90 H-mode base) are marked by bold points. (Here an average of the electron and ion temperatures was used so that the projections have somewhat lower Q values than in the table, which take advantage of the higher ion temperature and actual peak values.) Roughly speak-

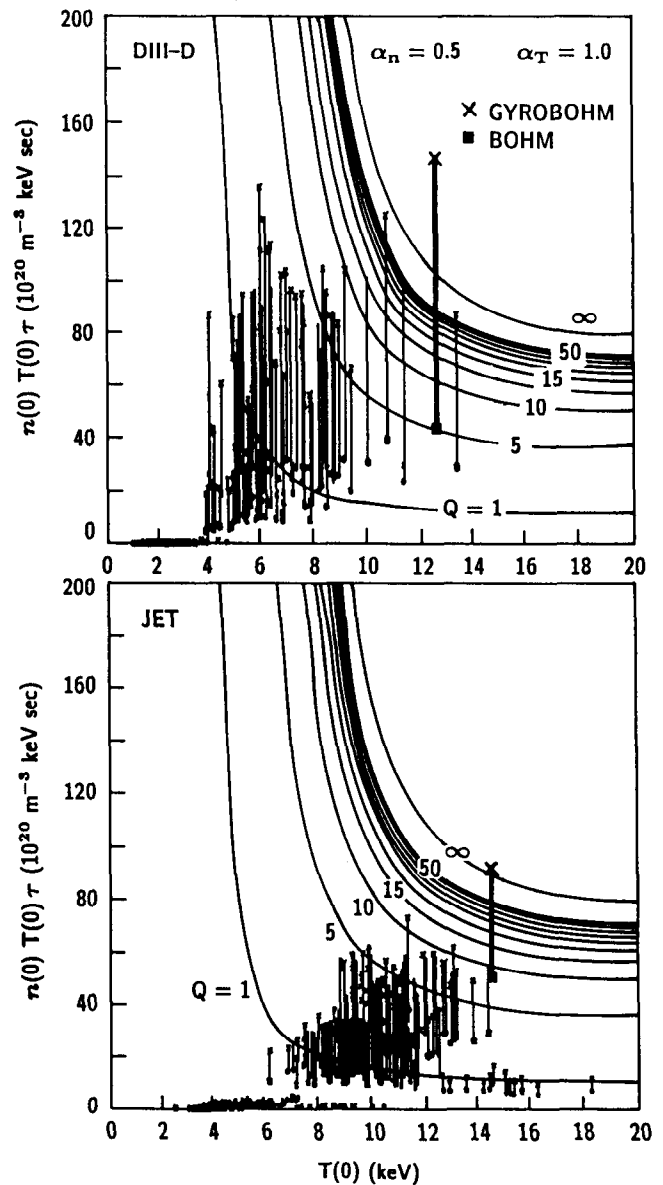


Fig. 3.3. BPX ignition parameter projections from (a) DIII-D and (b) JET dimensionally similar H-mode discharges in the ITER90 data base.

ing, the best shots project to $Q = 5$ or somewhat better by Bohm-like scaling and to very high Q or ignition for gyroBohm-like projections. The worst shots are simply at low power or low current. There are some important differences between DIII-D and JET data besides the fact that the DIII-D requires 100-fold projection of the ignition parameter and JET requires a 10-fold projection. The extrapolation from DIII-D to BPX requires a three-fold decrease in ρ_* while the extrapolation from JET to BPX requires a two-fold decrease. Thus, the Bohm-like and gyroBohm-like projections differ less for the latter. The DIII-D data are at higher β (up to $\beta/\beta_{crit} < 0.5$ for DIII-D

Table 3.1. B - a Projection at Fixed ν_* , β , q , κ , and B/a

Quantity	DIII-D		JET	
	Observed	BPX	Observed	BPX
Shot #	65747		20222	
B (T)	2.1	9	2.8	9
R (m)	1.7	2.6	3.1	2.6
a (m)	0.62	0.79	1.0	0.79
κ	2.1	2.1	1.9	1.9
I (MA)	2.0	9.2	4.2	10.0
$n_D(0)$ (10^{20} m^{-3})	1.1	7.0	0.56	2.9
τ_E (s)	0.21	0.51 [1.64] ^a	1.25	1.24 [2.23] ^a
$T_i(0)$ (keV)	4.5	12.9	8.3	16.7
$T_e(0)$ (keV)	3.5	10.0	7.6	15.3
$n_D(0)T_i(0)\tau_E$ ($10^{20} \text{ keV} \cdot \text{m}^{-3} \cdot \text{s}$)	1.0	45 [144] ^a	5.8	60 [107] ^a
β	0.041	0.041	0.024	0.024
$\nu_{* \text{ min}}$	0.083	0.083	0.027	0.027
Total power ^b (MW)	12	190 [58] ^a	7.2	36 [21] ^a
$\rho_{\text{BPX}}^* / \rho_{\text{Device}}^*$		0.31		0.56
Q		7 [∞] ^a		20 to 30 [∞] ^a

^a The first entry assumes Bohm-like scaling to BPX $nT\tau \propto B^{7/3}a^{5/3}$. The entries in square brackets assume gyroBohm-like scaling to BPX $nT\tau \propto B^3a^{5/2}$.

^b Combined alpha and auxiliary power: $P_{\text{aux}} = P_{\text{tot}} / [(Q/5) + 1]$.

and <0.3 for JET) and about 10-fold lower collisionality. Moderate Q (near 5) Bohm-like projections from DIII-D require substantially more auxiliary power than similar projections from JET. This may be an indication that the actual Cordey pass (minimal auxiliary power separatrix point) is nearer the low-collisionality JET projections.

In general, the data shown in Fig. 3.2 do not project to the optimal BPX operating point and so should be viewed as lower limits to the expected values of fusion Q . Typically, they have $q_{95} > 3.2$ and $\kappa_{95} < 2.0$, resulting in substantially reduced I_p . Since $nT\tau_E$ empirically scales approximately like I_p^2 , this implies a starting point that is far from optimal. Even the cases in Table 3.1 scale to plasma currents of 9.2 and 10.0 MA, well below the

BPX operating point of 11.8 MA. It should be emphasized that here we are illustrating the method with the unoptimized data at hand. We expect to receive more recent and better JET data soon. The BPX Physics R & D plan calls for the development and documentation of a data base of optimal shots for projection to the BPX parameters.

III.A.4. Theoretical and Empirical Model Projection: Comparisons and Sensitivity

The dimensionally similar projections with gyroBohm-like or Bohm-like scaling from the experimental points serve as lower bounds or bench points on the performance. To range freely over the n - T or β - ν_* parameter space, it is more convenient to directly use explicit theoretical and em-

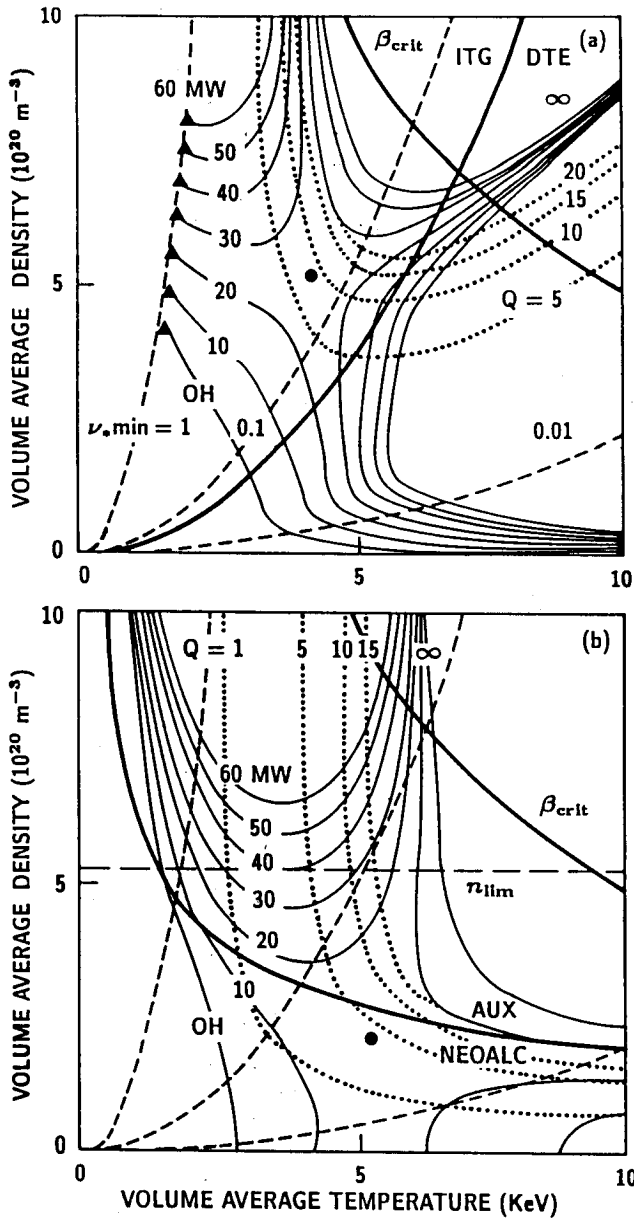


Fig. 3.4. Projected BPX power and Q -contour plots comparing a theoretical q -modified drift wave model (a) with the Goldston empirical model (b) using an H-mode enhancement factor of 2.5 (see Ref. 13).

piral models for confinement time. Not only do these have different scaling with respect to ρ_* , but also with β and ν_* . Ignition projections with both the theoretical models and the standard empirical models are treated in detail in Ref. 13. Here we only briefly compare and contrast them. Both have two components that are designed to describe the low-density ohmic neo-Alcator scaling regime and the high-density saturated regime, which evolves to L-mode (or H-mode) scaling with neutral beam

heating. For the theoretical model, the first component corresponds to the dissipative trapped electron (DTE) drift wave scaling and the second to the collisionless drift wave scaling of the ion temperature gradient (ITG) mode. Each of these theoretical confinement time scaling components is empirically modified by a q^2 factor to ensure the observed current scaling (as opposed to magnetic field scaling) in the L-mode regime and by a fast ion storage beam penetration factor P to obtain the L-mode density scaling. Although these q -modified drift wave models can fit the data almost as well as the statistical empirical models, the theoretical models are not unique. In particular, the neo-Alcator component could be equally well described by an Ohkawa-type c/ω_{pe} model with much less unfavorable temperature dependence ($\tau \propto n/T^{1/2}$ rather than $\tau \propto n/T^{7/2}$, in contrast to the empirical model that assumes no temperature dependence $\tau \propto n$).

Here we concentrate on the high-density, high-power L- (H-) mode scaling component. For the pure gyroBohm collisionless electrostatic drift wave model,

$$\tau_{dw} \propto \Omega^{-1} \rho_*^3 \nu_*^0 \beta^0 F_{dw}(q, R/a, b/a) P$$

and

$$nT\tau_{dw} \propto a^3 B^2 n/T^{1/2} F_{dw}^*(q, R/a, b/a) P,$$

where $P = (n_o/n)^{0.6}$, with n_o a machine-specific standard density, approximately describing the neutral beam heating effects. In projections with fixed penetration [e.g., with ion cyclotron resonance heating (ICRH)], $P = 1$. For the Goldston empirical model,

$$\tau_G \propto \Omega^{-1} \rho_*^{-1.5} \nu_*^{-0.25} \beta^{-0.75} a^{0.55} F_G(q, R/a, b/a)$$

and

$$nT\tau_G \propto a^{1.8} B^2 F_G^*(q, R/a, b/a),$$

where the explicit $a^{0.55}$ factor measures the deviation from dimensional consistency (i.e., $\tau_G \Omega$ cannot be expressed solely in terms of the relevant dimensionless plasma parameters.) By comparison, the apparently nearly identical Bohm-like ITER89-P scaling,

$$\tau_{ITER} \propto \Omega^{-1} \rho_*^{-2.05} \nu_*^{-0.275} \beta^{-0.525} a^{-0.075} \times F_{ITER}(q, R/a, b/a)$$

and

$$nT\tau_{ITER} \propto a^{1.70} B^{2.10} n^{0.2} F_{ITER}^*(q, R/a, b/a),$$

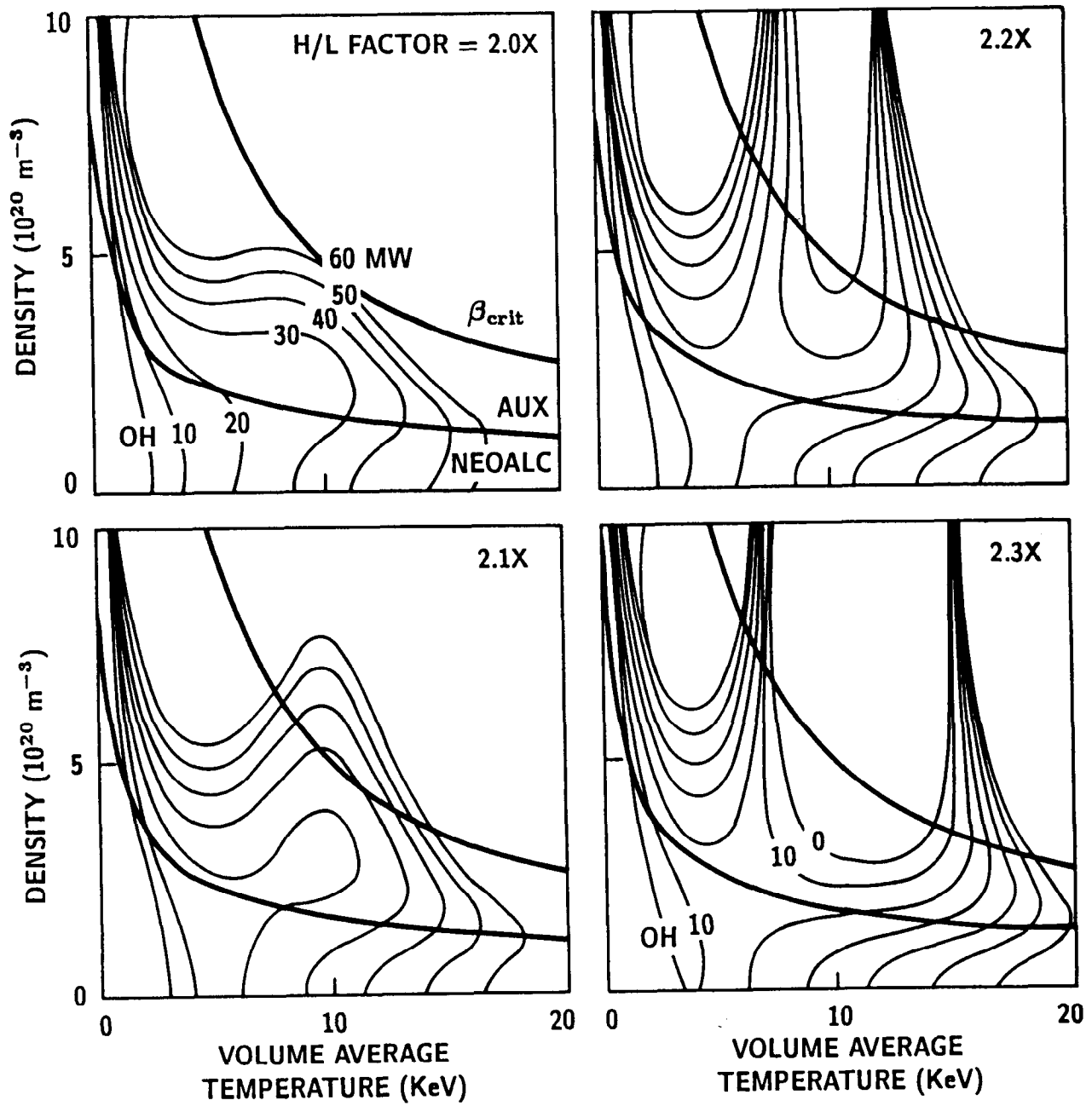


Fig. 3.5. Projected BPX power contour plots showing the “singular” behavior of the Goldston empirical model with the critical H-mode enhancement factor in the range 2.1 to 2.2.

is very nearly dimensionally consistent. Neither empirical model explicitly separates the parametric variability of beam penetration, resulting in little or no favorable density scaling of the ignition parameter. The posited penetration factor is replaced by unfavorable scaling with β and ν_* . From these formulas, it is clear that the theoretical model will tend to have optimal ignition points (and Cordey pass) at higher density and somewhat lower temperatures.

This is illustrated in Fig. 3.4, which compares a BPX n - T space power and Q -contours for the q -modified theoretical model¹² and the Goldston model ($\tau^{-2} = \tau_{auxheat}^{-2} + \tau_{neoclc}^{-2}$, where $\tau_{auxheat} = \tau_G$), both with an H/L enhancement factor of 2.5. Note that the drift wave model has the curious feature that the Cordey pass occurs at $Q = 9$. The Q -contours of the empirical model are almost independent of density at high density since $nT\tau$ is independent of density. Solid lines indicate the crossover between the DTE-ITG components and neo-Alcator auxiliary heating components of the models. In this example, the ignition contour is below the critical $\beta = 3.5I/aB$ and mostly in the regime governed by the ITG or L-mode (auxheat) component. The theoretical models¹² further posit that the density limit is governed by a radiative collapse that scales as $n_{lim} \propto B/Rq(P/POH)^{1/2}$ at fixed Z_{eff} ($= 1.5$). In contrast to the generally accepted limit $n_{lim} \propto I/a^2 \propto B/Rq$, higher power allows higher operating density, as shown by the triangles (in contrast to dashed line). Some power enhancement of the density limit has been observed in TFTR and JET L-modes (but published results are not available for H modes).

The optimal ignition parameter (e.g., maximum $nT\tau$ at the critical β) and, perhaps more importantly, the minimum required auxiliary power (power at the Cordey pass or power contour separatrix) P_{min} are very sensitive to the machine scales and the H/L enhancement factor C_τ , as well as the fit factor $f = \tau_{exp}/\tau_{fit}$ (for 90% of the data, $2^{-1/2} < f < 2^{1/2}$). For the collisionless drift wave theoretical model,

$$(nT\tau)_{max} \propto (f C_\tau)^{2.1} a^{2.5} B^{3.3}$$

and

$$P_{min} \propto (f C_\tau)^{-5} a^{-3} B^{-4}.$$

For the Goldston empirical model (or any model with $\tau \propto f C_\tau n^0 P^{-0.5\dots}$),

$$nT\tau \propto (f C_\tau)^2 a^{1.8} B^2$$

is independent of density and temperature. The power losses scale as n^2 like fusion gains. Hence,

there is no advantage to high-density operation, and the optimal point runs to the high-temperature maximum of fusion power. The ignition conditions and P_{min} have a "singular" behavior. This behavior is best illustrated by the extraordinary sensitivity of the power contours to small changes in the H/L enhancement factor shown in Fig. 3.5. The critical $C_\tau = 2.15$ in this case. The "standard" BPX assumptions of $1.85 \times$ ITER89-P L-mode scaling, as treated in detail in Sec. III.C, projects high- Q operation but not ignition, which requires a critical $C_\tau = 2.05$ rather than $C_\tau = 1.85$.

III.A.5. Conclusion

In conclusion, there are many unresolved differences between the theoretically motivated projection models and the purely empirical projection models. As we have noted, the theoretical models tend to have a more optimistic density dependence and a somewhat more pessimistic temperature dependence. Thus, the optimal (minimum power) path to ignition is at higher collisionality in the case of the theoretical models. The most important difference, however, is apparent in the dimensional analysis. The present theoretical models are gyroBohm-like, with a more favorable scaling to small relative gyroradius than the Bohm-like empirical models. This results in a significantly more optimistic field and size scaling of the ignition parameter for the theoretical models. Until further research can resolve this difference, it seems prudent to design BPX on the basis of the more conservative empirical models.

REFERENCES

1. B. B. KADOMSTEV, "Tokomaks and Dimensional Analysis," *Sov. J. Plasma Phys.* **1**, 295 (1985).
2. J. W. CONNOR, and J. B. TAYLOR, "Scaling Laws for Plasma Confinement," *Nucl. Fusion*, **19**, 1047 (1977); see also J. W. CONNOR, "Invariance Principles and Plasma Confinement," *Plasma Phys. Controlled Fusion*, **30**, 619 (1988).
3. B. A. CARRERAS and P. H. DIAMOND, "Thermal Diffusivity Induced by Resistive Pressure-Gradient-Driven Turbulence," *Phys. Fluids B*, **1**, 1011 (1989).
4. R. J. GOLDSTON, "Energy Confinement Scaling in Tokamaks: Some Implications of Recent Experiments with Ohmic and Strong Auxiliary Heating," *Plasma Phys. Controlled Fusion*, **26**, 87 (1984).

5. J. P. CHRISTIANSEN, J. G. CORDEY, and K. THOMPSON, "A Unified Physical Scaling Law for Tokamak Energy Confinement," *Nucl. Fusion*, (July 1990); see also "Unified Physical Scaling Laws for Tokamak Confinement," *Proc. 17th European Conf. Controlled Fusion and Plasma Heating*, Amsterdam, Netherlands, June 25-29, 1990, p. 797, European Physical Society (1990).
6. R. E. WALTZ, J. C. DeBOO, and M. N. ROSENBLUTH, "Scaling Dimensionally Similar Tokamak Discharges to Ignition," *Proc. 17th European Conf. Controlled Fusion and Plasma Heating*, Amsterdam, Netherlands, June 25-29, 1990, p. 126, European Physical Society (1990).
7. R. E. WALTZ, J. C. DeBOO, and M. N. ROSENBLUTH, "Magnetic-Field Scaling of Dimensionally Similar Tokamak Discharges," *Phys. Rev. Lett.*, **65**, 2390 (1990).
8. R. E. WALTZ, J. C. DeBOO, M. N. ROSENBLUTH, C. W. BARNES, R. J. GOLDSTON, D. K. JOHNSON, F. W. PERKINS, S. D. SCOTT, and M. C. ZARNSTORFF, "Tokamak Ignition Projections from Dimensionally Similar Discharges," *Proc. 13th Int. Conf. Plasma Physics and Controlled Nuclear Fusion Research*, Washington, D.C., October 1-6, 1990, Vol. II, p. 273, International Atomic Energy Agency.
9. R. J. GOLDSTON et al., "A Physics Perspective on CIT," *Proc. 17th European Conf. Controlled Fusion and Plasma Heating*, Amsterdam, Netherlands, June 25-29, 1990, p. 134, European Physical Society (1990).
10. L. R. GRISHAM et al., "The Scaling of Confinement with Major Radius in TFTR," *Proc. 17th European Conf. Controlled Fusion and Plasma Heating*, Amsterdam, Netherlands, June 25-29, 1990, p. 146, European Physical Society (1990).
11. F. W. PERKINS, "Issues in Tokamak/Stellarator Transport and Confinement Enhancement Mechanisms," PPPL-2708, Princeton Plasma Physics Laboratory (Aug. 1990).
12. R. E. WALTZ, R. R. DOMINGUEZ, and F. W. PERKINS, "Drift Wave Model Tokamak Ignition Projections with a Zero-Dimensional Transport Code," *Nucl. Fusion*, **29**, 351 (1989); see also *Proc. 12th Int. Conf. Plasma Physics and Controlled Nuclear Fusion Research*, Nice, France, October 12-19, 1988, Vol. 3, p. 369, International Atomic Energy Agency.

III.B. 1-1/2-DIMENSIONAL TRANSPORT SIMULATION USING THE MULTI-MODE MODEL

Glenn Bateman (PPPL)

C. E. Singer and J. Kinsey (University of Illinois)

The BPX design has been simulated with the $1\frac{1}{2}$ -dimensional BALDUR transport code^{1,3} using a combination of theoretically derived transport models, called the Multi-Mode Model.³⁻⁸ Version 5.10 of the Multi-Mode Model consists of a combination of effective thermal diffusivities resulting from the Dominguez-Waltz expression for trapped electron modes,⁹ the Hamaguchi-Horton expression for ion temperature gradient (η_i) modes,¹⁰ and the 1989 Carreras-Diamond expression for resistive ballooning modes.^{11,12} By changing only the boundary conditions, the same core transport model can be used to simulate both L-mode and H-mode plasmas. This and other versions of the Multi-Mode Model have been calibrated against TFTR, DIII-D, JET, PDX and ASDEX discharges.^{3,5-8} The model is described in detail in Sec. III.B.2.

III.B.1. BPX Simulation

This section describes the reference 1-1/2-dimensional BALDUR transport simulation CH01F4 of the BPX flattop using the Multi-Mode Model, with H-mode boundary conditions. The objective is to provide a self-consistent scenario for the evolution of plasma profiles and heating profiles using a theory-based transport model calibrated against experimental data. Note that power handling constraints are not considered in this simulation. Hence, the reference BPX scenario is not precisely duplicated.

In this simulation, 20 MW of centrally peaked auxiliary heating is applied to the ions for the duration of the 10-s flattop. (No attempt is made to provide consistency with divertor power handling capability.) The volume-averaged electron density is held fixed at $4.14 \times 10^{20} \text{ m}^{-3}$ using deuterium and tritium gas puffing (see Chap. VIII for pellet injection scenarios). This high density was chosen to maximize fusion output while remaining below the Greenwald density limit.¹³ The electron and ion temperatures are initially set at 2 keV and are then allowed to rise in response to the heating power and transport. At the end of the 10-s flattop, well after the last sawtooth crash, the results are characterized by Table 3.2.

The time evolution of the ion temperature and electron density profiles are shown in Figs. 3.6 and 3.7. The density is high enough to keep the elec-

Table 3.2. Simulation Results

\bar{n}_e	=	4.56×10^{20}	m^{-3}
$\langle n_e \rangle$	=	4.14×10^{20}	m^{-3}
n_{e0}	=	5.21×10^{20}	m^{-3}
T_{e0}	=	20.4	keV
T_{i0}	=	19.4	keV
τ_E	=	0.765	s
	=	$1.81\tau_{GL}$	Goldston scaling with $M^{0.5}$
	=	$1.79\tau_{ITER}$	ITER89-P scaling
P_α	=	96.7	MW of alpha heating
P_{aux}	=	20	MW ICRF all to ions
P_Ω	=	2.2	MW ohmic heating
P_{rad}	=	23.5	MW radiation
Q	=	21.75	(= $5P_\alpha / (P_{aux} + P_\Omega)$)
Z_{eff}	=	1.43	nearly uniform
$\langle \beta \rangle$	=	3.18 %	
flattop	=	10	s
r_{mix}/a	=	0.53	at last sawtooth crash
r_{inv}/a	=	0.36	($t = 9.35$ s)
q_0	=	0.6	sawteeth do not mix current
sawtooth period	=	1.3	s (prescribed, consistent with the Park-Monticello theory)

tron and ion temperatures nearly equal. The central temperature recovers rapidly after each sawtooth crash (flat ledges appearing every 1.3 s) and then saturates well before the next crash. The temperature profile outside of the sawtooth mixing region is relatively unaffected by the sawtooth activity. The resolution of the plot is not good enough to follow the heat pulse propagation after each crash. The density profile is essentially constant in time because it is so flat, which is consistent with the experience with many H-mode plasmas in DIII-D and JET.

The electron and ion thermal diffusivity profiles at the end of the simulation are shown in Figs. 3.8 and 3.9. The trapped electron mode and ion temperature gradient mode (η_i) contribute about equally to the core transport. Since $\nu_e^* \leq 0.05$ over most of the inner three-quarters of the plasma, the collisionless trapped electron mode dominates there. Resistive ballooning modes make a noticeable contribution only to the electron heat transport. All the modes are suppressed at the edge of the plasma due to the high shear there. The lumpiness of the thermal diffusivity profile is due to a

numerical instability associated with the threshold nature of the ion temperature gradient (η_i) mode that is controlled but not completely suppressed.

The time evolution of the heating power is shown in Fig. 3.10, together with the contributions from alpha heating (P_α), ion cyclotron resonance frequency (ICRF) heating (P_{aux}), and ohmic heating (P_{Ohmic}). At the end of the run ($t = 17.5$ s), there is 96.7 MW of alpha heating, 20 MW of auxiliary heating, and 2.2 MW of ohmic heating in the core of the plasma. The power losses are divided between 41.5 MW electron transport (conduction and convection are lumped together), 53.9 MW ion transport, and 23.5 MW radiative losses.

The time evolution of the ^4He (thermal ash) is treated in this simulation with the same empirical particle transport model as the other species (as described in Sec. III.B.2) with no recycling at the boundary. The resulting helium ash confinement time is a relatively short 1.4 s, and the profile saturates at a central value of $6.4 \times 10^{18} \text{ m}^{-3}$. Hence, the accumulation of helium ash has little effect on the fusion burn in this simulation. Work is under way to find theory-based particle

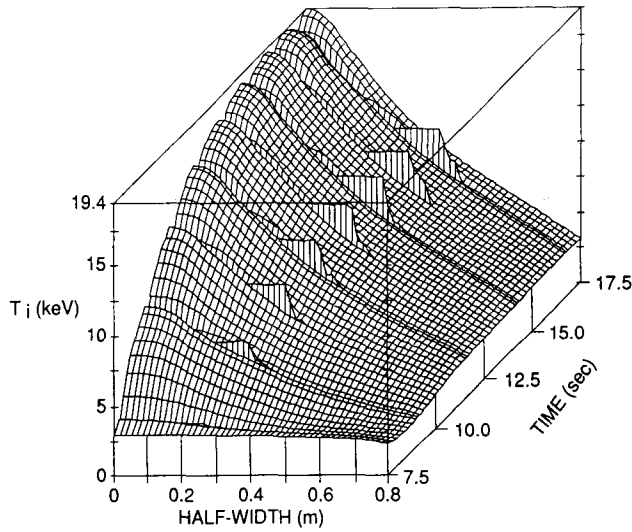


Fig. 3.6. Time evolution of the ion temperature profile during the BPX flattop in simulation ch01f4.

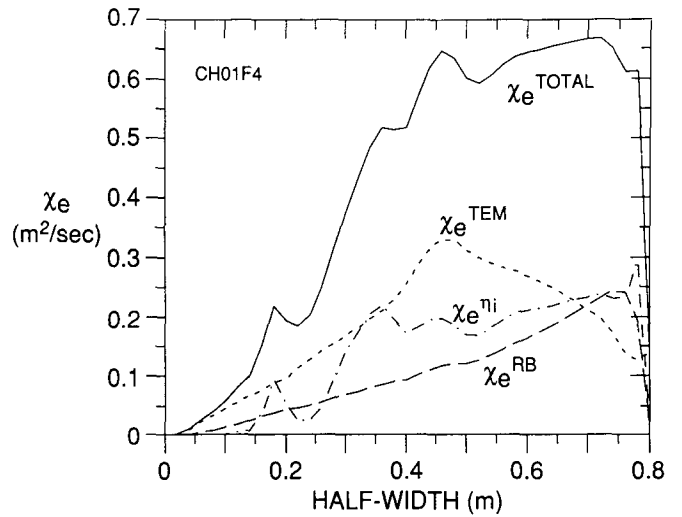


Fig. 3.8. Contributions to the effective electron thermal diffusivity profile at 17.2 s into the BPX simulation ch01f4.

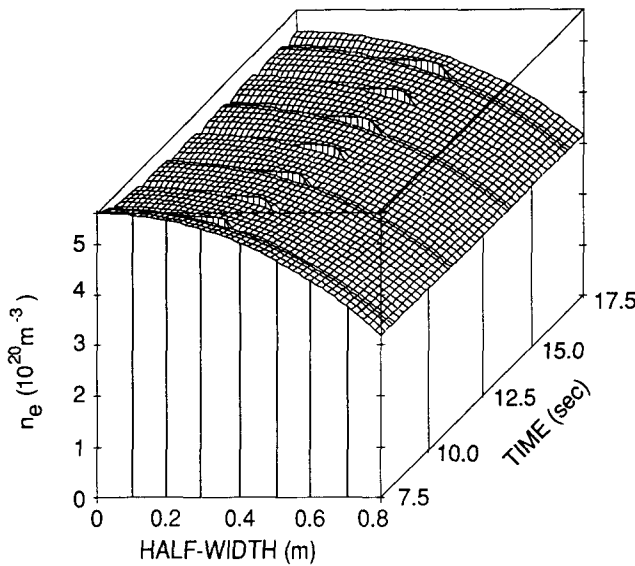


Fig. 3.7. Time evolution of the electron density profile during the BPX flattop in simulation ch01f4.

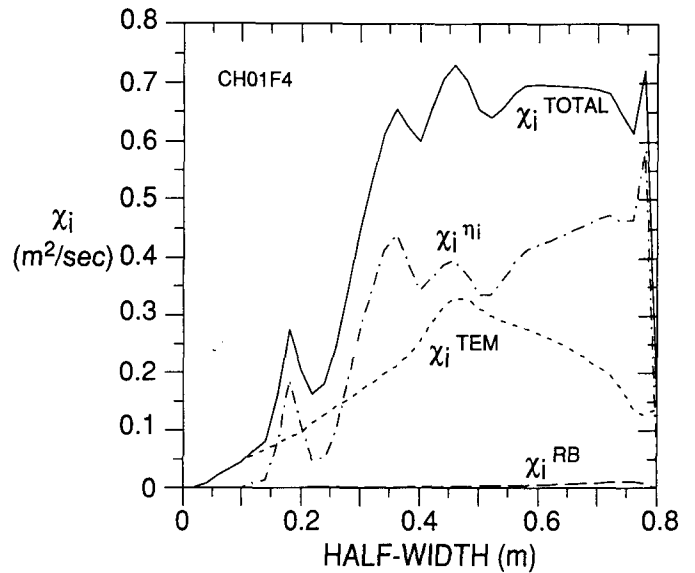


Fig. 3.9. Contributions to the effective ion thermal diffusivity profile at 17.2 s into the BPX simulation ch01f4.

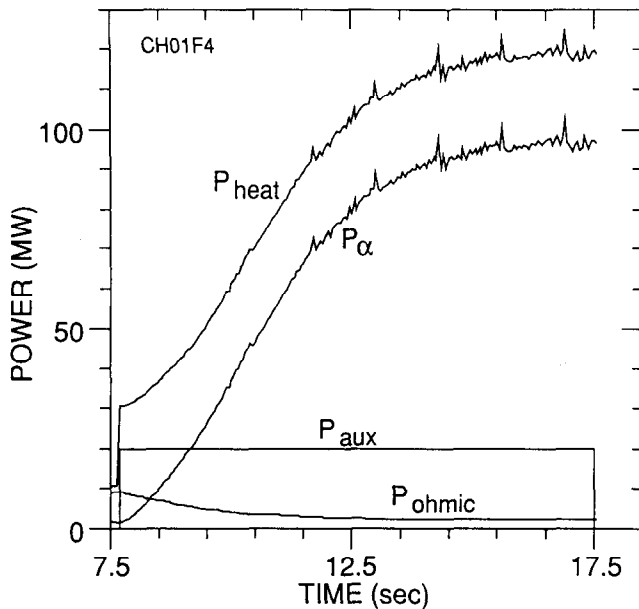


Fig. 3.10. Contributions to the heating power as a function of time during the BPX flattop in simulation ch01f4.

transport models that adequately approximate the experimentally observed density profiles.

The sawtooth oscillations are very broad in this simulation ($r_{mix}/a = 0.53$). This is consistent with the observation in DIII-D H modes that the sawtooth mixing radius follows the scaling $r_{mix}/a \approx 1/q_{95} + 0.27 \approx 0.58$ here. The sawtooth period is fixed at 1.3 s, in this simulation, consistent with the Park-Monticello model¹⁴ at $T_{e0} = 10$ keV. With ICRF and other superthermal particle effects, it may be possible to extend the length of sawtooth oscillations if needed.

III.B.2. Transport Model

The Multi-Mode Model of transport³⁻⁸ used in this simulation is a combination of theoretically derived transport models designed to approximate the thermal transport from the center to the edge of the plasma. This version of the Multi-Mode Model makes use of transport due to trapped electron mode and ion temperature gradient driven modes, which dominate in the core of the plasma, together with transport due to resistive ballooning modes, which dominate near the edge of the plasma.

Version 5.10 of the Multi-Mode Model is used in this paper. The trapped electron mode contribution is based on the model used by Dominguez and Waltz⁹ with modifications suggested by Rewoldt and Tang et al.^{15,16} The Hamaguchi and Horton¹⁰

theory is used for the ion temperature gradient driven turbulence (η_i) contribution. The Carreras and Diamond model is used for the resistive ballooning mode.^{11,12} This is the best and most completely developed set of theoretically derived transport models available at the present time. The coefficients and thresholds in these models have been adjusted to match the temperature profiles from experimental data.

Note that the resistive ballooning mode contribution to the Multi-Mode Model provides nearly Bohm-like diffusion while the other contributions are all gyroBohm-like.

The success of the Multi-Mode Model depends sensitively on the density profile. There has been some success with using the Multi-Mode Model to simulate particle as well as thermal transport in strongly beam-fueled plasmas. However, a unified theoretical model that reproduces observed L and H density profiles at both high and low collisionality is still under development. Fortunately, the electron density can be reasonably accurately determined by specifying any average density below an empirical density limit. Within this restriction, however, density profiles can still have some effect on the transport coefficients, which depend on various functions of the density gradient scale length. Consequently, the simulation is carried out using an empirical particle transport model that produces a density profile similar to the ones observed in JET and DIII-D H modes. The Multi-Mode Model was then used for the electron and ion thermal transport.

III.B.2.a. Trapped Electron Modes

The effective thermal diffusivities for the collisionless and dissipative trapped electron modes are similar to the forms used by Dominguez and Waltz⁹:

$$\chi_{e,i}^{DR} = 8.33 F_{e,i}^{DR} F_{\beta} F_{\kappa} \left(\frac{r}{R}\right)^{1/2} \times \frac{\rho_{e,i}^2 c_s}{L_{ni}} \left[1; \frac{0.1}{\nu_e'}\right]_{\min} \quad (3.1)$$

Here, $F_{e,i}^{DR}$ are input coefficients given below. The factor F_{β} is a finite beta correction that rises from 1.0 to 1.35 and then falls to 0.0 as beta is increased, with a form suggested by the simulations in Ref. 15:

$$F_{\beta} = \frac{1 + \beta'/\beta_c'}{1 + (\beta'/\beta_c')^3},$$

where $\beta' = \partial\beta/\partial r$, and $\beta_c' = \hat{s}/(1.7q^2R)$. The scaling with elongation, F_{κ} is described in Sec. III.B.2.d. The rest of the notation is described in

Tables 3.3 and 3.4. (SI units are used, with temperatures in keV.)

For the transition between dissipative and collisionless trapped electron modes, we have used the form $\left[1; \frac{0.1}{\nu_e^2}\right]_{\min}$ suggested by Ref. 16 rather than the form $\left[1; \frac{\omega_e}{\nu_{eff}}\right]_{\min}$ used by Dominguez and Waltz.⁹

These effective thermal diffusivities scale like

$$\chi_{e,i}^{DR} \sim T_e^{3/2} \left(\frac{r}{R}\right)^{1/2} \left|\frac{1}{n} \frac{\partial n}{\partial r}\right| \frac{A_i^{1/2}}{B^2} \times \left[1; \frac{T_e^2}{nqRZ} \left(\frac{r}{R}\right)^{3/2}\right]_{\min}. \quad (3.2)$$

In this simulation, the input coefficients were chosen to be $F_e^{DR} = 0.2$ and $F_i^{DR} = 0.2$, consistent with calibrations against TFTR L mode and JET H mode.⁸ Similar values were used in Refs. 5, 6, and 7 for simulations of L-mode and H-mode plasmas on DIII-D, JET, PDX, and ASDEX. This experience suggests that, as further calibrations are made, these values are likely to stay in the range $0.1 < F_{e,i}^{DR} < 0.3$. Since the trapped electron mode thermal diffusivities are such strongly nonlinear functions of temperature, the results are relatively insensitive to the choice of these coefficients.

III.B.2.b. Ion Temperature Gradient (η_i) Mode

The Hamaguchi-Horton theory¹⁰ is used for the effective electron and ion thermal diffusivities:

$$\chi_{e,i}^{IG} = F_{e,i}^{IG} F_{\kappa} \frac{\rho_{fc}^2}{L_n} \max(\eta_i - \eta_i^{th}, 0) \times \exp[-\min(5L_n, 4L_{Ti})/L_s], \quad (3.3)$$

where $F_{e,i}^{IG}$ are input constants. The threshold η_i^{th} is based on the results of Dominguez and Rosenbluth¹⁷:

$$\eta_i^{th} = \max(1.0, 5.0|L_n/R|). \quad (3.4)$$

Since η_i is typically small near the center and rises to large values near the edge of the plasma, these effective thermal diffusivities typically rise to their maximum value about two-thirds of the way from the center of the plasma, and then, because of the positive temperature dependence in these scalings, the effective thermal diffusivities fall to small values near the edge. Hence, the η_i mode typically fills in between the trapped electron modes in the core of the plasma and the resistive ballooning modes at the edge.

In this simulation, the input coefficients for this model were chosen to be $F_e^{IG} = 3.0$ and $F_i^{IG} = 6.0$, consistent with calibrations against TFTR L mode and JET H mode.

III.B.2.c. Resistive Ballooning Mode

The Carreras-Diamond theory is used for the effect of resistive ballooning modes^{11,12}:

$$D^{RB} = f_{dia} \Lambda^2 \frac{\beta R q^2}{\sqrt{2} L_p \hat{s}} \frac{r^2}{\tau_R} \sim \frac{d(nT)}{dr} \frac{R q^2 Z_{eff} \Lambda^2}{T_e^{3/2} B^2 \hat{s}},$$

$$\chi_i^{RB} = F_i^{RB} F_{\kappa} D^{RB},$$

$$\chi_e^{RB} = F_{e1}^{RB} F_{\kappa} f_{dia} \frac{\Lambda^{4/3}}{2^{13/6}} \left(\frac{\tau_{hp}}{\langle n \rangle \tau_R}\right)^{2/3}$$

$$\times \left(\frac{\beta R q^2}{L_p}\right)^{4/3} \frac{v_e r^2}{\hat{s} R}$$

$$+ F_{e2}^{RB} F_{\kappa} D^{RB}$$

$$\sim \frac{n_e^{1/3} [d(nT)/dr]^{4/3} r^{2/3} R q^{8/3}}{T_e^{1/2} B^{10/3} \hat{s}},$$

where

$$\Lambda \equiv \frac{2}{3\pi} \ln \left[256 \hat{s}^2 L_p \left(\frac{\hat{s}}{\langle n \rangle}\right)^4 \right]$$

is typically ≈ 7 . There is a strong effect from diamagnetic stabilization of these modes,

$$f_{dia} = \left[1 + \left(\frac{0.01 \mu_o \omega_{ci} \rho_i^3}{\eta \beta q^2 L_{ni}} \right)^2 \right]^{-1/6},$$

which typically decreases two to three orders of magnitude from the edge to the center, reflecting the nonfluid nature of the modes in a hot plasma. Since many modes are allowed in the high-shear region near the edge of the plasma, we have chosen the root-mean-square toroidal mode number $\langle n \rangle$ to be 2.

The first contribution to the resistive ballooning mode effective electron thermal diffusivity comes from parallel transport along magnetic field lines with magnetic flutter. This contribution typically peaks a few centimeters in from the edge of the plasma and then becomes small at the very edge of TFTR plasmas, because $[d(nT)/dr]^{4/3}$ diminishes faster than $T_e^{1/2}$. The second contribution comes from $E \times B$ interchange, which produces comparable electron and ion, thermal and particle, transport. It is important to retain this contribution because it increases monotonically out to the edge of the plasma.

In this BPX simulation, the coefficients were chosen to be $F_{e1}^{RB} = 1.0$, $F_{e2}^{RB} = 4.0$, and $F_i^{RB} = 4.0$, consistent with calibrations against TFTR L mode and supershots.

Table 3.3. Notation: Fundamental Variables

Symbol	units	Meaning
r	m	minor radius (half-width) of flux surface
R	m	major radius of flux surface
B	tesla	toroidal magnetic field at major radius R along flux surface
M	kg	average hydrogenic ion mass
Z		Z_{eff}
n_e	m^{-3}	electron density
n_i	m^{-3}	thermal ion density
T_e	keV	electron temperature
T_i	keV	ion temperature
q		magnetic q value

III.B.2.d. Effect of Plasma Elongation

The theories available at this time do not include the effects of plasma elongation. Hence, for the moment, we are using an empirical scaling with elongation. It is surprising to note that energy confinement scalings of the form

$$\tau_E \propto \kappa^{0.5} I_p$$

imply a thermal diffusivity scaling with local elongation $\kappa(r)$ like

$$\chi \propto [(1 + \kappa(r)^2)/2]^{-2}.$$

Calibrations carried out by Singer et al. find that either $\chi \propto \kappa(r)^{-4}$ or $\chi \propto \kappa(r)^{-2}$ are consistent with experimental data from DIII, with a slight leaning toward $\chi \propto \kappa(r)^{-4}$.

For the simulations described here, all contributions to the thermal diffusivity were scaled with local elongation using

$$F_\kappa = [(1 + \kappa(r)^2)/2]^{-2}.$$

Since the results are quite sensitive to this scaling with elongation, better theoretical guidance and more calibrations against experiments are needed.

III.B.2.e. Particle Transport

Most of the calibration effort to date has gone into adjusting the model for thermal diffusivity. What calibration there has been of the Multi-Mode Model particle transport has compared with experiments in which there is significant neutral beam

injection fueling or with ohmic discharges. So far, no simulations have been carried out using theoretically based particle transport models with radio-frequency (RF) heating and intermittent pellet injection fueling.

With this in mind, a simple empirical particle transport model was chosen for the simulations presented here. In particular, the diffusivity and pinch velocity

$$D = 0.5[1 - 0.5(r/a)^2] \text{ m}^2/\text{s}$$

and

$$v = 0.3r/a^2 \text{ m/s}$$

produce essentially the density profile

$$n(r) = (n_0 - n_{edge})[1 - (r/a)^2]^{0.5} + n_{edge}.$$

These transport coefficients were applied to all four charged-particle species (deuterium, tritium, helium, and carbon). A rather high edge pedestal condition n_{edge} was used, as described below. Only gas fueling was used in this simulation.

III.B.2.f. Boundary Conditions

The boundary in these simulations corresponds to approximately the 95% flux surface, a few centimeters in from the separatrix and scrape-off layer, the region treated in detail in Chap. I. H modes are generally characterized by a steep density gradient (a pedestal) and, to a lesser extent, temperature gradient in this edge region. The boundary conditions for the simulations are assumed to refer

Table 3.4. Notation: Derived Variables

Symbol	Name (units)	Formula
ω_{ci}	ion cyclotron frequency (s^{-1})	$eB/(m_p A_i)$
β	beta	$(2\mu_o k_b/B^2)(n_e T_e + n_i T_i)$
ω_{pe}	plasma frequency (s^{-1})	$[n_e e^2/(m_e \epsilon_o)]^{1/2}$
v_e	electron thermal velocity (m/s)	$(2k_b T_e/m_e)^{1/2}$
v_i	ion thermal velocity (m/s)	$(2k_b T_i/m_p A_i)^{1/2}$
c_s	sound speed (m/s)	$[k_b T_e/(m_p A_i)]^{1/2}$
v_A	Alfvén speed (m/s)	$B/(\mu_o n_e m_p A_i)^{1/2}$
β_θ	poloidal beta	$\beta(q/\epsilon)^2 = 4.027 \times 10^{-22} (n_e T_e + n_i T_i) B^{-2} \epsilon^{-2} q^2$
$\ln(\lambda)$	Coulomb logarithm	$37.8 - \ln(n_e^{1/2} T_e^{-1})$
ν_{ei}	electron collision frequency (s^{-1})	$4(2\pi)^{1/2} n_e (\ln \lambda) e^4 / [3(4\pi \epsilon_o)^2 m_e^{1/2} (k_b T_e)^{3/2}]$
η	Spitzer resistivity (Ohm-m)	$\nu_{ei}/(2\epsilon_o \omega_{pe}^2)$
ν_{eff}	effective collision frequency (s^{-1})	ν_{ei}/ϵ
ν_e^*	electron collisionality	$\nu_{ei} q R / (\epsilon^{3/2} v_e)$
L_n	density scale length (m)	$-n_e / (\partial n_e / \partial r)$
L_{ni}	ion scale length (m)	$-n_i / (\partial n_i / \partial r)$
L_{T_j}	$T_e; T_i$ scale lengths (m)	$-T_e / (\partial T_e / \partial r); -T_i / (\partial T_i / \partial r)$
η_i		L_n / L_{T_i}
L_p	pressure scale length (m)	$-\beta / (\partial \beta / \partial r) \equiv \beta / \beta'$
\hat{s}	shear	$(r/q)(\partial q / \partial r)$
ρ_i	ion gyroradius (m)	$= v_i / \omega_{ci}$
$\rho_{\theta i}$	poloidal gyroradius (m)	$= \rho_i q / \epsilon$
ρ_s		$= c_s / \omega_{ci}$
k_\perp	wave number (m^{-1})	$\approx 0.3 / \rho_s$
ω_e^*	diamagnetic frequency (s^{-1})	$k_\perp \rho_s c_s / L_n$
τ_{hp}	poloidal Alfvén time (s)	$= R / v_A$
τ_A	Alfvén time (s)	$= q \tau_{hp}$
ϵ	inverse aspect ratio	$= r / R$

to the top of this pedestal, eliminating the complexity of the separatrix and scrape-off layer in the simulation.

The calculation of the density pedestal boundary condition is taken from Ref. 18, Eqs. (22) and (24), which can be written

$$n_{ped} = n_b [-1 + \sqrt{1 + (\bar{n}/n_b)^2}],$$

where

$$n_b = 1.4 \times 10^{19} B \text{ m}^{-3}.$$

For the BPX simulation with $\bar{n}_e = 3.0 \times 10^{20}$, we find $n_{ped} = 2.0 \times 10^{20} \text{ m}^{-3}$ (again, at the top of the

pedestal). Such high ratios of n_{ped}/\bar{n} are common in present-day experiments. These density conditions are fixed throughout the simulation.

According to the model used in Ref. 18, the temperature pedestal boundary condition depends upon plasma heating power passing through the boundary. For example, the pedestal temperatures are estimated to be 3.46 keV with 100 MW of alpha heating. These estimates put the temperatures at the 95% flux surface far out of the range of present-day experiments. As a compromise, 2 keV was chosen as the boundary temperature used in simulation CH01E4.

Finally, the shear at the boundary of the simulation was enhanced to account for the proximity of the separatrix (since the VMOMS equilibrium code used in BALDUR is not accurate near the separatrix). The enhanced shear is given by

$$s = |(r/q)(dq/dr)| + \left[\frac{1}{|1-r/a| |\ln(4/\sqrt{|1-r/a|})|} - \frac{1}{\ln 4} \right].$$

These boundary conditions have the effect of partially suppressing the resistive ballooning mode at the edge of the plasma, producing the kind of thermal barrier observed in H-mode experiments.

III.B.2.g. Sawtooth Model

An estimate of the sawtooth period is based on the Park-Monticello model¹⁴:

$$\begin{aligned} \tau_{\text{sawtooth}} &\approx 0.009 R_m^2 T_{e0}^{3/2} / Z_{\text{eff}} \text{ s} \\ &\approx 1.3 \text{ s for BPX with } T_{e0} = 10 \text{ keV,} \end{aligned}$$

where T_{e0} refers to the central electron temperature after a sawtooth crash. Since this has not yet been automated within the BALDUR code, a fixed period of 1.3 s was used in the BPX simulation.

The Kadomtsev model is used to redistribute temperature and density profiles during each sawtooth crash. However, the current density is not redistributed, in order to be generally consistent with experimental observations that the magnetic q value at the magnetic axis remains well below unity while sawtooth oscillations are taking place. This model leaves considerable magnetic shear within the sawtooth mixing region, which stabilizes ideal ballooning modes as the central plasma reheats between each sawtooth crash. However, the inconsistency between this model and the Park-Monticello model needs to be resolved, and, in general, improved sawtooth models need to be developed.

It should be noted that the sawtooth mixing region covers nearly 50% of the half-width of the plasma in this simulation. Experimental observations from DIII-D by Snider et al. would suggest that sawtooth mixing region covers closer to 60% of the plasma half-width in similar DIII-D discharges (with same q_{95}). This is an indication that the current (and temperature) profile may be narrower than predicted by the model used here. Future refinements to the model will attempt to address this issue. Also, it should be noted that no attempt was made in this simulation to freeze in a broader current profile, which would make the sawtooth mixing region still narrower for a current penetration time.¹⁹⁻²¹

REFERENCES

1. C. E. SINGER et al., "BALDUR: A one-dimensional plasma transport code," *Comp. Phys. Commun.*, **49**, 275 (1988).
2. G. BATEMAN, "Simulation of Transport in Tokamaks," in *Computer Applications in Plasma Science and Engineering*, A. T. Drobot, Ed., p. 381, Springer-Verlag, New York (1991).
3. C. E. SINGER, "Theoretical Particle and Energy Flux Formulas for Tokamaks," *Comm. Plasma Phys. Controlled Fusion*, **11**, 165 (1988).
4. J. SHEFFIELD, "Tokamaks Transport in the Presence of Multiple Mechanisms," *Nucl. Fusion*, **29**, 1347 (1989).
5. C. S. SINGER, E.-S. GHANEM, G. BATEMAN, and D. P. STOTLER, "Multimode Model of Tokamak Transport," *Nucl. Fusion*, **30**, 1595 (1989).
6. M. H. REDI and G. BATEMAN, "Transport Simulations of TFTR Experiments to Test Theoretical Models for χ_e and χ_i ," *Nucl. Fusion*, **31**, 547 (1991).
7. C. E. SINGER et al., "Predictive Modelling of Tokamak Plasmas," *Proc. 13th Int. Conf. on Plasma Physics and Controlled Nuclear Fusion Research*, Washington, D.C., October 1-6, 1990, CN-53/D-4-6, International Atomic Energy Agency.
8. G. BATEMAN, "Theory-Based Transport Simulations of TFTR L-Mode Temperature Profiles," Princeton Plasma Physics Laboratory report PPPL-2764 (1991), to appear in *Phys. Fluids*.
9. R. R. DOMINGUEZ and R. E. WALTZ, "Tokamak Transport Code Simulations with Drift Wave Models," *Nucl. Fusion*, **27**, 65 (1987).
10. S. HAMAGUCHI and W. HORTON, "Fluctuation Spectrum and Transport from Ion Temperature Gradient Driven Modes in Sheared Magnetic Fields," Report IFSR 383, University of Texas, Institute for Fusion Studies (Aug. 1989).
11. B. A. CARRERAS and P. H. DIAMOND, "Thermal Diffusivity Induced by Resistive Pressure Gradient Driven Turbulence," *Phys. Fluids*, **B1**, 1011 (1989).
12. B. A. CARRERAS, L. GARCIA and P. H. DIAMOND, "Theory of Resistive Pressure Gradient Driven Turbulence," *Phys. Fluids*, **30**, 1388 (1987).
13. M. GREENWALD, J. TERRY, S. WOLFE, S. EJIMA, M. BELL, S. KAYE, and G. H. NEILSON, "A New Look at Density Limits in Tokamaks," *Nucl. Fusion*, **28**, 2199 (1988).

14. W. PARK and D. A. MONTICELLO, "Sawtooth Oscillations in Tokamaks," *Nucl. Fusion*, **30**, 2413 (1990).
15. G. REWOLDT, W. M. TANG, and R. J. HASTIE, "Collisional Effects on Kinetic Electromagnetic Modes and Associated Quasilinear Transport," *Phys. Fluids*, **30**, 807 (1987).
16. W. M. TANG, G. REWOLDT, and L. CHEN, "Microinstabilities in Weak Density Gradient Tokamak Systems," *Phys. Fluids*, **29**, 3715 (1986).
17. R. R. DOMINGUEZ and M. N. ROSENBLUTH, "Local Kinetic Stability Analysis on the Ion Temperature Gradient Mode," *Nucl. Fusion*, **29**, 844 (1989).
18. C. E. SINGER, G. BATEMAN, and D. P. STOTLER, "Boundary Conditions for OH, L, and H-mode Simulations," PPPL-2527, Princeton Plasma Physics Laboratory (June 1988).
19. G. BATEMAN, "Delaying Sawtooth Oscillations in the Compact Ignition Tokamak," PPPL-2373, Princeton Plasma Physics Laboratory Laboratory (Sept. 1986).
20. D. P. STOTLER, D. POST, and G. BATEMAN, "Sawtooth Effects in Elongated, High-Current Tokamak Reactors," *Fusion Technol.*, **14**, 1304 (1988).
21. D. P. STOTLER and G. BATEMAN, "Time-Dependent Simulations of a Compact Ignition Tokamak," *Fusion Technol.*, **15**, 12 (1989).

III.C. THE EMPIRICAL BASIS FOR PROJECTING BPX PERFORMANCE

R.J. Goldston (PPPL), R. E. Waltz (GA)

III.C.1. Early Scaling Relations

Early theoretical work on electrostatic drift wave turbulence in tokamaks provided the basis for the first theory-based projections of tokamak reactor requirements. The so-called "six-regime model" included a range of dissipative and collisionless trapped particle mode projections, drawing the conclusion¹ in 1974 that tokamaks with plasma currents in the range of 10 MA would be required to obtain ignition. While the theoretical analyses that underpinned these projections have subsequently evolved as represented in the previous sections, and much experimental data has now accumulated, it is remarkable to observe how close those projections were to our present empirical understanding, as discussed in this section.

In the late 1970s, a wide range of ohmically heated tokamak experiments began producing data, and a clear trend became apparent that energy confinement improved with plasma density. This was most dramatically demonstrated on the Alcator-A tokamak, a high-field device with a wide range of accessible density. Combining results from many tokamaks, and choosing the simplest overall size scaling, a so-called "Alcator" scaling² was proposed: $\tau_E \propto na^2$. Dimensional constraints similar to those discussed in Sec. III.A coupled with a more direct analysis of the ohmically heated confinement data base, however, suggested a L^3 size scaling with greater dependence on R than a (Ref. 3). For conservatism, the International Tokamak Reactor (INTOR) group adopted the na^2 scaling in its design work, and "INTOR" scaling became synonymous with "Alcator" scaling. Initial neutral beam heating results on ISX-B and at low density on PLT supported this scaling, even in auxiliary heated regimes.

By 1980, however, auxiliary heating results at high power and high plasma density began to show clear degradation from Alcator scaling on PLT and ISX-B. Subsequent results from DIII, PDX, and the ASDEX tokamak in Germany provided enough additional data that in 1983 a reliable confinement scaling relation could be deduced for devices with strong auxiliary heating.⁴ The experimental results spanned only a small range in size, current, and heating power ($R = 1$ to 1.6 m, $I_p = 0.1$ to 0.5 MA, $P < 5$ MW), but the close correspondence of the power, current, density, and field scalings between the different devices made it possible to compare results from device to device with confidence,

in order to obtain an overall size scaling. The resulting confinement scaling relation was approximately $\tau_E \propto I_p R^{3/2} \kappa^{1/2} P^{-1/2}$, very nearly consistent with dimensional constraints, despite the fact that such constraints had not been imposed in advance. Using $P \propto \langle nT \rangle R a^2 \kappa / \tau_E$, one could deduce $\langle nT \rangle \tau_E \propto (I_p R / a)^2$. The constant of proportionality was such that ignition would require a device with $I_p R / a \sim 70$ MA — a daunting prospect. At this same time, however, initial results from the ASDEX tokamak indicated that an enhanced confinement regime, the so-called “H mode,” could be accessed in divertor tokamaks. This regime exhibited confinement about two times higher than the standard “L-mode” regime, showing promise that the $I_p R / a$ required for high- Q operation could perhaps be reduced by a factor of ~ 2 .

In the period up to 1986, L-mode data accumulated from the next generation of large tokamaks: TFTR, JET in Europe, and JT-60 in Japan; devices with $R = 2.5$ to 3 m, $I_p = 1$ to 5 MA, and neutral beam heating power up to 20 MW. The new L-mode data showed remarkable agreement with the 1983 “Aachen” scaling relation, as can be seen in Fig. 3.11. Indeed, the mean error of the new data with respect to the scaling relation derived from the smaller, lower current devices was -4% , and the root-mean-square error was 11.5%, demonstrating the reliability of this technique of extrapolation. During this time period, investigations of the H mode continued on ASDEX, D-III, and other medium-scale devices, and other approaches to enhanced confinement were also developed.

A key event in 1986 was the achievement of the H mode on JET. The observation that the standard features associated with a strong transport barrier near the edge of the plasma led again to a factor ≈ 2 improvement in confinement in such a large, high-power device, similar to what had been found in smaller, low-power devices, was of critical importance. An *additive* effect on W_{tot} or τ_E similar in absolute magnitude to what had been observed on ASDEX would have been negligible on JET or BPX. The fact that the effect was indeed *multiplicative* on JET as on ASDEX opened the door for use of H-mode confinement enhancement on high- Q devices such as BPX.

Another important event in 1986 was the discovery on TFTR of a new enhanced confinement mode, “supershots,” associated with high-power neutral beam injection and low wall recycling of neutrals. These discharges had very peaked density profiles and confinement times as high as three times L mode. Direct extrapolability of this approach to BPX and to other high- Q devices is problematic since neutral beams with adequate particle

energy to penetrate to the core of such devices are too energetic to provide significant fueling relative to heating or current drive. However, the combination of radio-frequency (RF) heating and pellet injection (available on BPX) may provide the key elements of supershots. Results from JET and TFTR in developing this RF + pellets variant of peaked density profile enhanced performance operation are promising.

III.C.2. ITER89-P L-Mode Scaling Relation

With the accumulation of L-mode data from the next larger generation of tokamaks, the ITER physics group encouraged the activity of developing a new L-mode data base and sponsored workshops to analyze the new data. The BPX physics team participated in this activity, but the direct access to international data afforded by the ITER process was invaluable. A number of different approaches were taken to analyzing the data; the approach that has garnered the most public acceptance involved, in essence, a negotiating process in which the “home teams” argued for aspects of the scaling relation that best fit their most trusted data. This gave rise to the ITER89-P scaling relation⁵:

$$\tau_E^{ITER89-P} = 0.038 A_i^{0.5} I_p^{0.85} R^{1.2} a^{0.3} \times \kappa^{0.5} \bar{n}_{19}^{-0.1} B_T^{0.2} P^{-0.5}, \quad (3.5)$$

where the units are seconds, atomic mass units, mega-amperes, meters, meters, 10^{19} m^{-3} , Tesla, and megawatts. The term “ \bar{n}_{19} ” in this and in subsequent scaling expressions refers to the electron density in units of 10^{19} m^{-3} line averaged along a central chord. Again, without specific effort, this scaling relation was found to be in excellent agreement with dimensional constraints. Evaluating the expression for typical high- Q BPX parameters: $A_i = 2.5$, $I_p = 11.8$ MA, $R = 2.59$ m, $a = 0.795$ m, $\kappa = 2.2$, $\bar{n} = 4 \times 10^{20} \text{ m}^{-3}$, $B_T = 9$ T, and $P = 80$ MW, we find $\tau_E = 0.533$ s. As expected, this is inadequate to support a high enough temperature to produce nearly 80 MW of alpha heating power. The factor ~ 2 associated with H-mode confinement, or other enhanced confinement modes, is required to achieve the performance required on BPX.

A number of different statistical approaches have been taken to the ITER L-mode data base. In particular, it was observed that despite overall similarities, different tokamaks had slightly different internal scalings with respect to P_{heat} , I_p , \bar{n} , and B_T . The differences were found to lie outside of the range of expected statistical variation, imply-

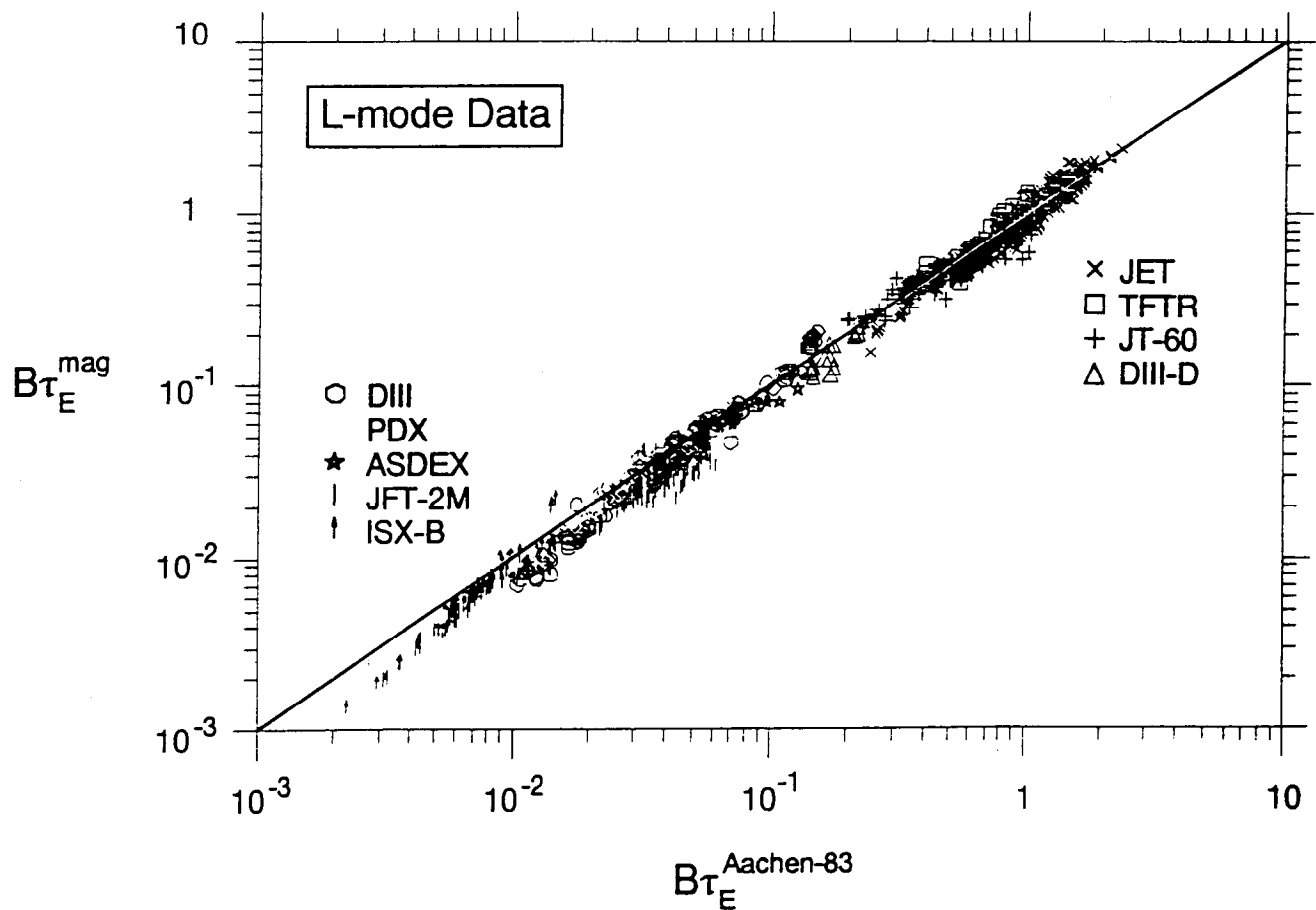


Fig. 3.11. Energy confinement time inferred from magnetic data plotted against the 1983 "Aachen" confinement scaling for the L-mode data base from nine tokamaks operated during the 1980s.

ing that the different tokamaks represented different statistical populations. Analysis taking this observation into account⁶ via a "random coefficients" method gave rise to a scaling relation extremely close in form to the 1983 version. The predicted BPX confinement time, $\tau_E = 0.587$ s, however, is still reasonably close to the ITER89-P value (10% above), while the value based on the original "Aachen" scaling relation, $\tau_E = 0.534$ s, is extremely close to the ITER89-P value. Direct linear regression fit to the subset of the data base corresponding to tokamaks with $a > 0.35$ m selects the most relevant and best diagnosed data, and gives a similar result, $\tau_E = 0.496$ s (7% below ITER89-P). All of the data in this data base were measured via magnetic techniques, which of necessity include stored energy from the fast ions used for plasma heating. This stored energy was estimated and subtracted from the magnetically measured stored energy prior to regression analysis.⁷ The result gives a projected confinement, $\tau_{E,th}^* (\equiv W_{th}/P_{inj}) = 0.491$ s, but because $\sim 10\%$ of

the neutral beam power was likely lost by charge-exchange and on bad orbits before heating the plasma, this implies a thermal confinement time, $\tau_{E,th} (\equiv W_{th}/P_{heat})$, very similar to the ITER89-P value.

In summary, the ITER89-P scaling gives results for BPX that are very similar to results obtained from the L-mode data base through a number of different methods. It is the most reliable L-mode scaling for characterizing the highest quality data from each of the tokamak experiments, due to the process through which it was generated, and thus we use it as our L-mode benchmark. In general, the L-mode confinement prediction for BPX is robust, but disappointing.

III.C.3. ITER H-Mode Data Base

Based on the success of the L-mode data base work, the ITER physics group sponsored a similar effort⁸ with respect to divertor H-mode data, and once more the BPX physics team participated.

H-mode data were accumulated from a range of divertor tokamaks in the United States, Europe, and Japan. Measurements of total stored energy were provided from fits to magnetohydrodynamic (MHD) equilibrium and from measurements of the plasma diamagnetic effect. "Bad" data were discarded on the basis of a number of complex criteria, and a "standard" list of some 1239 data sets was developed. The comparison of the mean result from each machine with the ITER89-P scaling is given in Table 3.5. In this case, we have added an additional constraint on the steady-state nature of the discharges, $dW/dt < 0.2P_{heat}$, and also a constraint to eliminate very high q discharges, $q_{95} < 5.0$.

For further analysis, the H-mode data base working group chose to standardize on "MHD" data, since no diamagnetic data were available from PBX-M or PDX. In the case of JET, however, they chose to use diamagnetic data, because this data showed less scatter. In the case of ASDEX, they "reconstructed" MHD-like data from the more reliable diamagnetic data and from an estimate of fast ion anisotropy. With this data selection, which coincidentally in each case favored the higher measurement of stored energy, they found a mean multiplier of $2.11 \times \text{ITER89-P}$ in the full "standard" set. We adopt an alternative approach, which uses the more reliable (and less scattered) diamagnetic data where available and also uses in each case the form of magnetic data that minimizes the fast ion stored energy. We employ MHD data only for PDX and PBX-M, which had pure perpendicular and mixed tangential and perpendicular injection, respectively, and diamagnetic data for all of the other tokamaks, which had varying degrees of tangential injection. This approach gives a multiplier of $1.86 \pm 0.31 \times \text{ITER89-P}$, using the constraints applied to Table 3.5. The data are shown in Fig. 3.12. The uncertainty in predicting the mean L-mode performance (not including shot-to-shot scatter) of BPX has been estimated⁹ at $\pm 17\%$. Summing this result in quadrature with a 17% uncertainty in projecting the ratio of H- to L-mode confinement, we obtain an overall uncertainty of 24% in the projected BPX confinement time by this "two-step" approach.

The H-mode working group also examined the "internal" scalings with P_{heat} , I_p , \bar{n} , and B_T for each tokamak. The result was disheartening, in that the scalings differed substantially between tokamaks, making the construction of an overall scaling relation highly uncertain. In particular, direct fits to the data base gave a strong scaling with magnetic field ($\tau_E \propto B^{0.91}$), greater than observed in any of the individual tokamaks, and greater than observed in controlled scans. The scaling law ob-

tained by direct fit to the "standard" data set is

$$\tau_E^{ITERH-ST} = 0.021 A_i^{0.5} I_p^{0.55} R^{2.22} a^{0.19} \times \kappa^{0.7} \bar{n}_{19}^{0.17} B_T^{0.91} P^{-0.55} \quad (3.6)$$

with the same units as Eq. (3.5). Evaluated for BPX parameters, this gives $\tau_E = 1.98$ s, an unbelievable $3.7 \times \text{ITER89-P}$.

The data base was then constrained to data free of edge-localized modes (ELMs), since it was believed that some of the machine-to-machine differences could arise from differences in the characteristics of ELMs. Examination of this data set again, however, revealed difficulties with the B scaling. Individual machine regressions, as well as the overall regression result, both showed substantial scaling with B , but controlled parameter scans tend to show weaker scaling with B . Thus, the working group compromised on fixing a scaling of $B^{0.15}$ and developed a unified scaling law for the ELM-free H-mode:

$$\tau_E^{ITER90H-P} = 0.082 A_i^{0.5} I_p^{1.02} R^{1.6} \kappa^{-0.19} B_T^{0.15} P^{-0.47}, \quad (3.7)$$

with the same units as Eq. (3.5). Evaluated for BPX parameters, this gives $\tau_E = 1.12$ s, $2.11 \times \text{ITER89-P}$. BPX, like JET, may be able to operate for moderate pulse lengths in ELM-free H modes, but it would also be desirable to explore the physics of ELM'y H modes. Confinement is estimated to be $\sim 20\%$ lower in ELM'y H modes than in ELM-free cases, giving $1.69 \times \text{ITER89-P}$ for BPX parameters.

The "random coefficients" model has recently been applied to the full "standard" H-mode data set.¹⁰ In studying the data set, it was observed that a significant subset of the JET data is clustered at low P_{heat}/I_p , as can be seen in Fig. 3.13. This parameter corresponds roughly to auxiliary heating power divided by initial ohmic heating power, since ohmic loop voltages tend to be ~ 1 V. When P_{heat}/I_p is constrained to be > 2.5 , the different machine scalings are brought into better alignment. The result of the random coefficients analysis is

$$\tau_E^{RCH} = 0.07094 A_i^{0.5} I_p^{0.889} R^{1.344} a^{0.233} \times \kappa^{0.317} \bar{n}_{19}^{0.105} B_T^{0.207} P^{-0.486}, \quad (3.8)$$

with the same units as Eq. (3.5). Evaluated for BPX parameters, this gives $\tau_E = 1.21$ s, 2.27 times ITER89-P, in this case for a mix of ELM'y and ELM-free discharges as might be observed in BPX. The 1σ prediction uncertainty for the mean device performance is estimated at $\pm 26\%$.

Table 3.5. H-Mode Confinement Time Enhancement Factors

Device	$\tau_E^{DIA} / \tau_E^{ITER89-P}$	$\tau_E^{MHD} / \tau_E^{ITER89-P}$
JET	2.10 ± 0.28	1.86 ± 0.35
DIII-D	1.70 ± 0.13	1.70 ± 0.21
ASDEX	2.23 ± 0.22	(2.73 ± 0.30)
PBX-M	—	2.05 ± 0.26
PDX	—	1.56 ± 0.33
JFT-2M	1.51 ± 0.16	1.79 ± 0.21
	1.88 ± 0.34	1.79 ± 0.18
		$(1.95 \pm 0.42 \text{ including ASDEX})$

(Uncertainty ranges given for individual devices indicate shot-to-shot scatter, while “bottom-line” range indicates device-to-device scatter.)

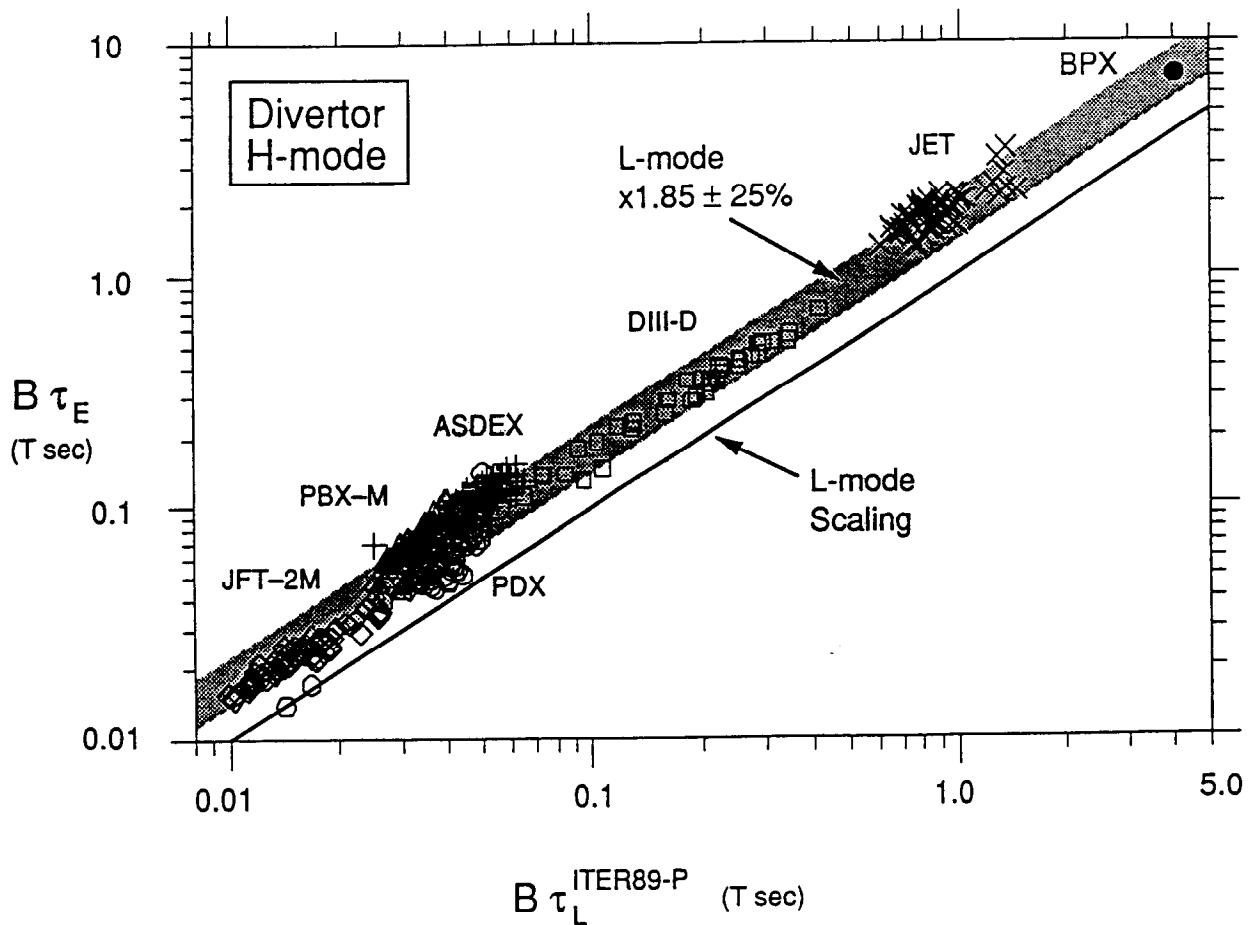


Fig. 3.12. Experimentally measured divertor H-mode confinement times plotted against the ITER89-P L-mode confinement scaling. Type of data (MHD versus diamagnetic) selected to minimize fast ion stored energy. The extrapolation to BPX is shown in the upper right-hand corner.

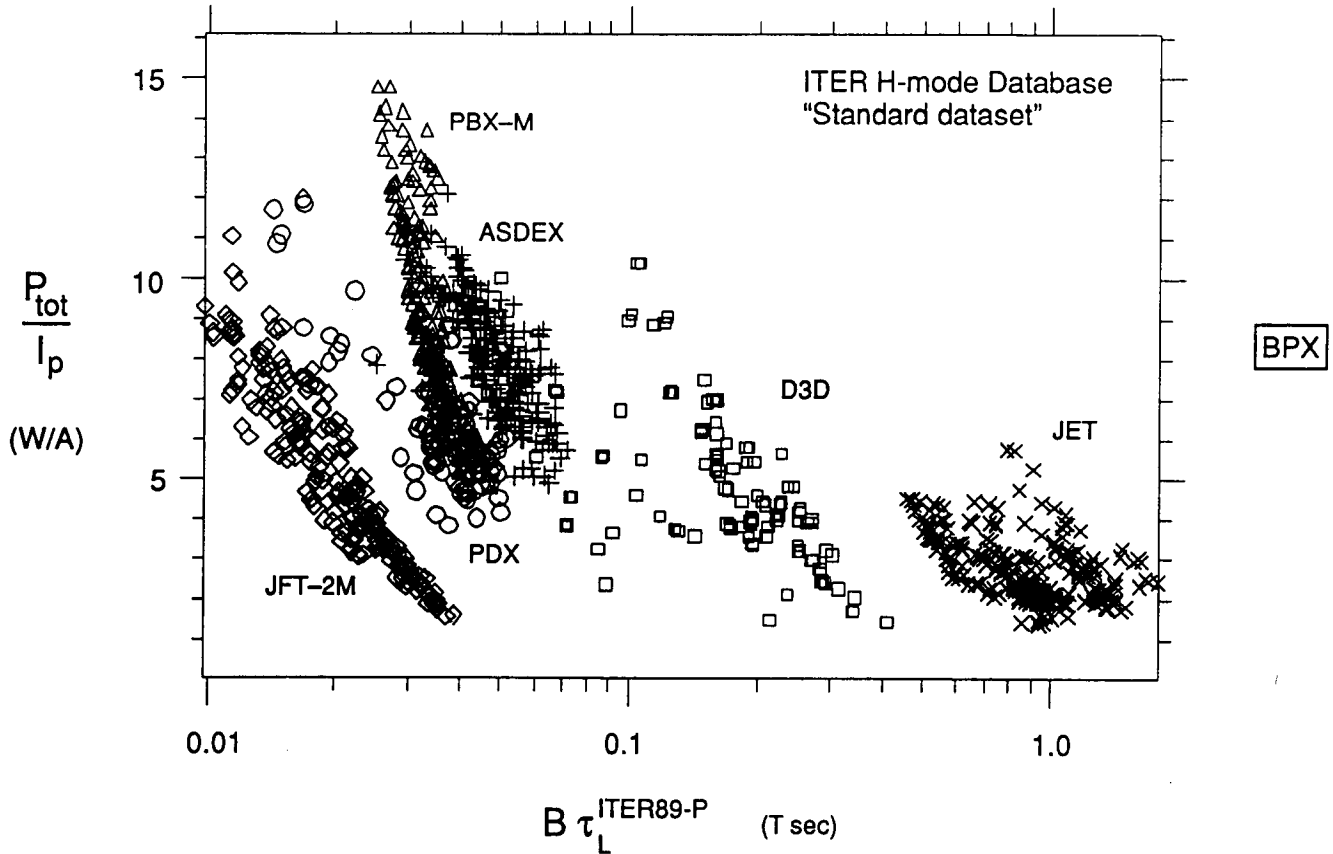


Fig. 3.13. Heating power divided by plasma current plotted against the ITER89-P L-mode confinement scaling for the ITER H-mode standard data set.

A somewhat different approach to the H-mode confinement scaling problem was taken by the JET and DIII-D groups.¹¹ They compared data from experiments including discharges with all parameters held fixed, except size, between the two devices. Because DIII-D tends to experience strong ELMs during the steady-state portion of their discharges, while JET does not, it was necessary to compare results during the rise phase ($dW/dt \sim 0.3P_{heat}$). During this phase, the fast ion component can be relatively large (as high as $\sim 50\%$ in some of the DIII-D discharges), so the fast ion stored energy was subtracted, giving a $\tau_{E,th}^*$, as discussed above. No account was taken for fast ion losses leading to a reduction of the heating power. Attributing the observed size scaling to major radius variation (R/a was fixed), fixing the uncertain \bar{n} and B scalings to both be zero, and taking over A_i and κ scalings from ITER89-P, the resulting scaling expression is

$$\tau_E^{D3D-JET} = 0.0559 A_i^{0.5} I_p^{1.03} R^{1.48} \kappa^{0.5} P^{-0.46}, \quad (3.9)$$

with the same units as Eq. (3.5). Evaluated for BPX parameters, this gives $\tau_E = 0.907$ s, 1.7 times ITER89-P, in this case for thermal confinement in the ELM-free rise phase of the discharge. It must be noted, however, that the absence of any B or \bar{n} scaling is not derived from this data and may significantly affect the projection for BPX. Furthermore, the lack of correction for losses of fast ion heating efficiency may result in a significant underestimate of the overall confinement time.

To summarize, it is clear that H-mode scaling studies are rather more difficult to perform than L-mode studies. However, the fact that devices ranging in size, field, and power from JFT-2M to JET all see factors of ~ 2 enhancement relative to L mode provides confidence that similar performance will be obtained on BPX. It is still too early to settle on an accepted H-mode scaling, but the ranges of the projections, the estimated uncertainty of projection, and the range of H/L multipliers obtained suggest that a reasonable estimate of BPX performance is to take $\tau_E = 1.85 \tau_E^{ITER89-P}$, with a 1σ uncertainty range of $\pm 25\%$ for the mean perfor-

mance of the device, corresponding to an ITER89-P multiplier in the range of 1.4 to 2.3. This estimate should be viewed as conservative in that it takes no credit for advances in understanding or technique in the ten years leading up to BPX operation. It is also worth noting that the new scaling relations based on H-mode data, however preliminary, tend on average to be more optimistic than $1.85 \times \tau_E^{ITER89-P}$.

It is interesting to put the estimated range of uncertainty ($\pm 25\%$) in the context of dimensionless scaling arguments, as discussed in Sec. III.A. BPX is planned to operate with absolute time scales such as τ_E , magnetic skin time, and flattop pulse length very similar to those of JET. Thus, in dimensionless time, $\Omega_c \tau_E$ the extrapolation of confinement is in proportion to the magnetic fields: $9/3.4 = 2.6$. A 25% uncertainty corresponds to a range of 1.95 to 3.25 in this extrapolation. On the basis of the results shown in Fig. 3.12, representing eight years of work on H-mode tokamaks, this seems to be quite reasonable.

III.C.4. The H Mode in BPX

As we have just seen, high- Q operation in BPX requires H-mode operation with a critical H/L enhancement factor. All existing divertor tokamaks with deuterium operation have achieved H-mode operation. However, at present, we have no fully reliable machine parameter design criterion for ensuring H mode at high field and high density. Consequently, the extrapolability of the H mode is a key issue addressed in the BPX R&D Plan.

Since the H-mode transition originates at the edge, a local rather than global criterion most likely will be needed. Nevertheless, a first attempt¹³ at global scaling for the power threshold from a world data base is given by

$$P_{th}/S = 12B \text{ kW m}^{-2} \text{ T}^{-1}$$

for single-null diverted deuterium plasmas. For BPX at 9 T, this corresponds to ~ 13 MW. Recent JET ion cyclotron resonance frequency (ICRF) H modes require < 2.4 MW/T (or $14 \text{ kW m}^{-2} \text{ T}^{-1}$) (Ref. 17). Figure 3.14 illustrates the long extrapolation to high field (and high density). Clearly, an improved world data base is needed; in particular, high-field Alcator-C-Mod H-mode operation will provide valuable data. Several notes should be made: The high threshold points in Fig. 3.14 are from nondiverted operation or hydrogen operation. In the case of DIII-D hydrogen into deuterium beam heating, there was substantial pollution from hydrogen beam gas, and pure deuterium beam data are not available because the threshold

is below one source (2.5 MW). Further, the threshold power has a large hysteresis, so that the L/H transition can be obtained at lower field (and density) followed by ramps to higher values.

Specific devices disagree in some respects with this overall B field scaling of power per unit area, again suggesting that global parameters poorly reflect edge conditions:

JET	$P_{th} \propto B$	
DIII-D	$P_{th} \propto B n I^0$	$T_{edge}^{crit} \propto B$
ASDEX	$P_{th} \propto B^0 n^0 I^0$	$T_{edge}^{crit} \propto F(q)$
JFT2-M	$P_{th} \propto B n^{-1} I^{-1}$	

This prompts some theoretical notes on the H-mode power threshold scaling. Dimensional analysis (at fixed q , b/a , and R/a) ignoring atomic physics and divertor variables and using $P_{th} \propto n^x B^y a^z$ imposes the constraint $z = 2x + (5/4)y - (3/4)$. Thus, power per unit surface may intuitively be the key parameter, but $P_{th} \propto B a^{1/2}$ (not $B a^2$) follows from insisting $x = 0$ and $y = 1$. Fortunately, the size scaling is not of much importance in scaling from DIII-D and JET to BPX. There are several critical temperature gradient bifurcation theories proposed to explain the H mode, but they do not have the observed scaling with B . For example,¹⁵ η_e stabilization of collisional drift wave transport gives a bifurcation to ion-temperature-gradient (ITG) drift wave transport (or more likely neoclassical transport) with $P_{th} \propto n q^2 B^{-1.5}$, assuming $T_{edge} \propto B$. There is, however, no clear evidence that the L/H transition is to larger η_e values at the edge. Or, in another example, Biglari et al. have applied the Biglari, Diamond, and Terry¹⁶ theory of rotational stabilization of ITG turbulent transport. This allows a bifurcation from ITG to neoclassical transport with $P_{th} \propto n^{3.3} q^{2.3} B^{-3.5}$ (again assuming $T_{edge} \propto B$). Perkins¹⁷ posited an ion orbit drift loss flux theory with $P_{th} \propto n T V_{drift} \propto n T^2 c / (eBR) \propto n B$ (assuming $\nu_* > 1$ and $T_{edge} \propto B$). Unfortunately, this theory has no bifurcation mechanism nor an explanation as to why $T_{edge} \propto B$.

In summary, the scaling of the H-mode threshold power is difficult to determine with high accuracy, and theory does not yet provide even rough guidance. Present estimates indicate that BPX has a margin of a factor of ~ 1.5 in power, which could be increased to a factor as high as 4 with the upgrade to 50 MW of heating power. This determination leaves out the fact that BPX can begin heating at reduced magnetic field in a single-null configuration and that D-T plasmas are likely to have a lower H-mode power threshold than D-D plasma,

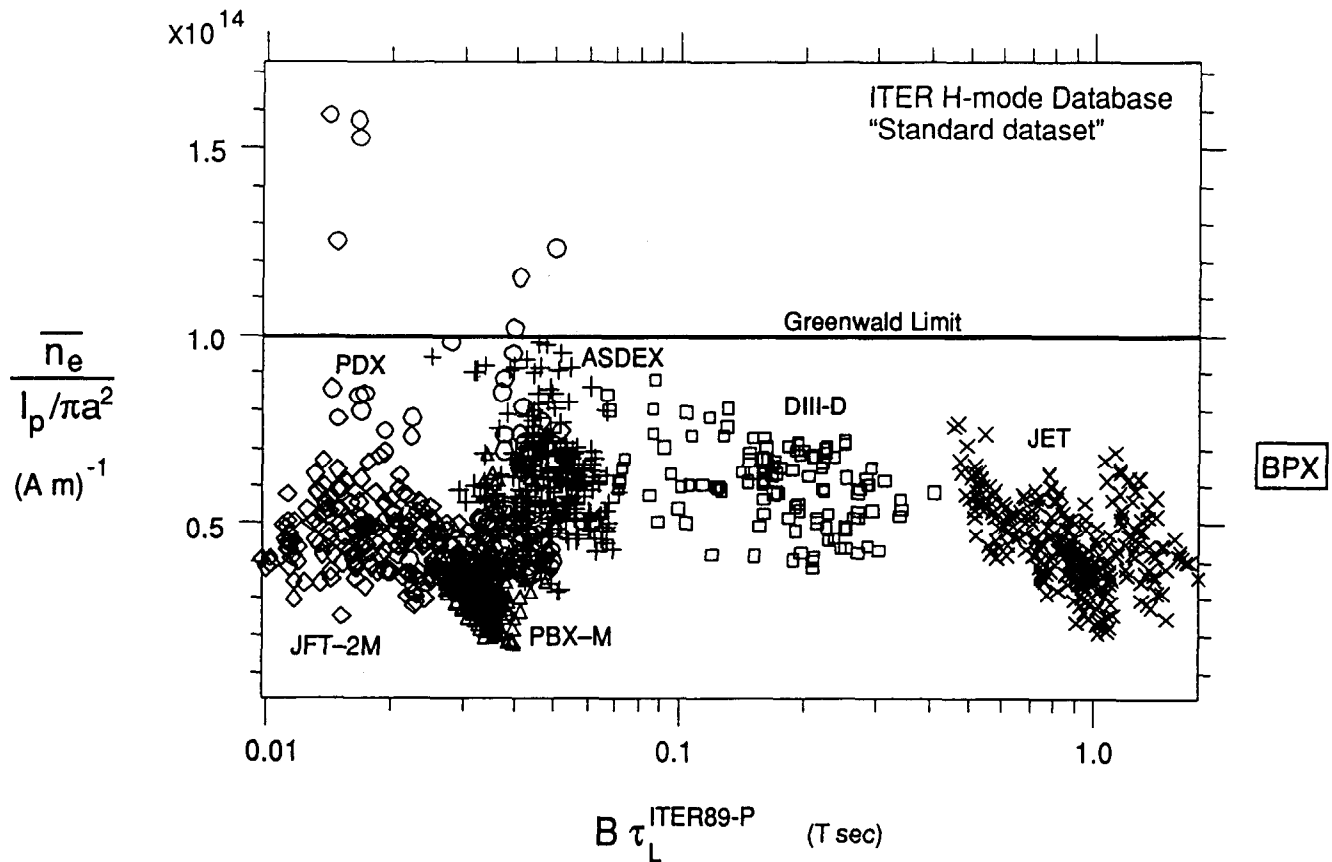


Fig. 3.15. Line-averaged electron density normalized to the Greenwald limit plotted against the ITER89-P L-mode confinement scaling for data from six tokamaks operated during the 1980s.

permit core fueling, without disturbing the edge particle or energy balance greatly. Between shots, helium GDC (Ref. 12) will be available to further reduce wall desorption, if required. This provides considerable confidence that the H-mode density operating range planned for BPX will be readily accessible.

III.C.6. Performance Projection Ranges for BPX

A number of key parameters govern the projected fusion performance of BPX. These are the energy confinement time, density and temperature profile shapes, impurity content, helium ash content, and alpha heating efficiency. The projected values of these parameters and their ranges of uncertainty are presented in this section. In general, it is well recognized that it is possible to create discharges with degraded confinement (e.g., due to low- m tearing modes) or poor plasma purity (e.g., due to improper plasma handling technique), and

indeed some such discharges will certainly be generated on BPX. The projections presented here, however, represent the performance expected on the *best hundreds of high-power discharges*. We have reviewed above the status of projecting H-mode energy confinement for BPX. We take as our standard projection $1.85 \times$ ITER89-P scaling, with 1σ uncertainty of $\pm 25\%$.

The density profile shape plays an important role in determining the overall fusion reactivity, even for fixed energy confinement time. H modes often have very flat density profiles, especially when they are subjected to strong edge fueling. On the other hand, we have argued that desorption of neutrals from the walls of BPX should be a weaker effect than in DIII-D or JET, and pellets are projected to penetrate well into even high-temperature BPX plasmas. Thus, we take the range of uncertainty for the density profile to be from perfectly flat to parabolic, with mean shape square-root parabolic.

For the temperature profile shapes, we assume

a central flat region from $r = 0$ to the estimated $q = 1$ surface at $r/a = 1/q_{95}$. Outside of $q = 1$, the temperatures are taken to fall linearly to zero at $r = a$. This shape is a good approximation to observations on DIII-D at low q and has in general been observed on low- q sawtooth tokamaks. We do not assign significant uncertainty to this profile shape since tokamak electron temperature profiles have a remarkable "consistency." We assume $T_i = T_e$, appropriate for the high-density operation anticipated in BPX. At $Q = 5$, alpha heating to electrons will equal ICRF heating to the ions.

It is to be noted that neither the density nor temperature profile shapes explicitly allow for an edge pedestal. As more H-mode profile data from low- q elongated plasmas become available, it would be appropriate to use some form of mean experimental profile shapes for projecting BPX fusion reactivity. For the time being, however, we note three items that suggest these profiles are reasonably conservative. First, the range of pressure peakedness we are assuming is very modest, $\sim 2 < P_o/\langle P \rangle < 3$. Even at very low q , JET observes pressure peaking of ~ 3 in the H mode (Ref. 18). Second, the projected sawtooth repetition time in BPX well exceeds projected global confinement time, so one should anticipate significant time-averaged profile peaking within the $q = 1$ radius, even in the presence of sawteeth. This peaking is observed in the simulations reported elsewhere in this paper. Ignoring such central peaking represents some modest conservatism, which may offset the absence of density and temperature edge pedestals in the model profiles. Finally, it has been observed in simulations of BPX operation that if the auxiliary heating is applied before the end of the current ramp, the $q = 1$ surface can be maintained well inside of $r/a = 1/q_{95}$ for the duration of the heating pulse, resulting in significantly more peaked temperature profiles.

The proper range of Z_{eff} to project for BPX is difficult to determine. Ohmically heated tokamaks operating at the high density anticipated in BPX have frequently obtained Z_{eff} as low as 1.2. On the other hand, present-generation, low-density, high-power tokamaks typically achieve $Z_{eff} = 2$ only with considerable difficulty. JET, however, using beryllium gettering to reduce oxygen impurities, has obtained Z_{eff} as low as 1.6, even at a plasma density of $4 \times 10^{19} \text{ m}^{-3}$ and beam powers up to 18 MW. BPX will have the capability to provide a boron coating on the first wall, which should similarly reduce oxygen influx. Thus, we take $Z_{eff} = 1.65$ as the mean projection for BPX, with a 1σ uncertainty range of ± 0.35 . The dominant impurity species is taken to be fully ionized carbon.

The helium ash content in BPX is taken to be equal to the full amount of helium produced — no helium pumping is assumed. This means that the mean helium density rises at $\sim 3 \times 10^{18} \text{ m}^{-3} \cdot \text{s}$ when $P_{fus} = 500 \text{ MW}$. We assume that the helium density profile shape is the same as that of the D-T fuel.

The last topic of importance for determining the fusion performance of BPX, and in some sense the most interesting, is the alpha heating efficiency. For the purposes of Sec. III.D, we simply insert $P_{aux} + P_{oh} + P_{\alpha} - P_{br}$ into the ITER89-P scaling relation for P . This amounts to assuming that the alpha heating efficiency will be the same as that of the external auxiliary heating systems represented in the data base. The centrally peaked bremsstrahlung radiation P_{br} , which was negligible in previous experiments, is counted against the other forms of heating before inclusion in the scaling relation. These assumptions should be conservative in that the bremsstrahlung radiation profile is rather broad in H-mode plasmas, and the alpha heating is calculated, on the basis of classical effects, to be nearly 100% efficient and highly peaked on axis. The circumstances under which these assumptions are not conservative, of course, correspond to conditions where alpha-driven instabilities cause substantial losses of alpha power or plasma containment. The discovery and investigation of such instabilities, however, would constitute success with respect to a major fraction of the mission of the device, so we do not include these in the "downside risk."

REFERENCES

1. S. O. DEAN et al., "Status and Objectives of Tokamak Systems for Fusion Research," WASH-1295, UC-20, U.S. Government Printing Office (1974).
2. D. L. JASSBY, D. R. COHN, and R. R. PARKER, "Reply to 'Comments on the Paper, 'Characteristics of High-Density Tokamak Ignition Reactors,'" *Nucl. Fusion*, **16**, 1045(1982).
3. W. PFEIFFER and R. E. WALTZ, "Empirical Scaling Laws for Energy Confinement in Ohmically-Heated Tokamaks," *Nucl. Fusion*, **19**, 51 (1979).
4. R. J. GOLDSTON, "Energy Confinement Scaling in Tokamaks: Some Implications of Recent Experiments with Ohmic and Strong Auxiliary Heating," *Plasma Phys. Controlled Fusion*, **26**, 87 (1984).
5. P. N. YUSHMANOV et al., "Scalings for Tokamak Energy Confinement," *Nucl. Fusion*, **30**, 1990 (1990).

6. K. S. REIDEL and S. M. KAYE, "Uncertainties Associated with Extrapolating L-Mode Energy Confinement to ITER and CIT," *Nucl. Fusion*, **30**, 731 (1990).
7. R. J. BICKERTON and R. J. GOLDSTON, Private Communication (1989).
8. J. G. CHRISTANSEN et al., "A Global Energy Confinement H-mode Database for ITER," Draft Report (1990).
9. K. S. REIDEL, "On Dimensionally Correct Power Law Scaling Expressions for L-Mode Confinement," submitted to *Nucl. Fusion*.
10. K. S. REIDEL, Report 121, New York University Magneto-Fluid Dynamics Division (Feb. 1991).
11. D. P. SCHISSEL et al., "H-Mode Energy Confinement Scaling from the DIII-D and JET Tokamaks," *Nucl. Fusion*, **31**, 73 (1991).
12. G. L. JACKSON et al., "Reduction of Recycling in DIII-D by Degassing and Conditioning the Graphite Tiles," *J. Nucl. Mater.*, **162-164**, 489 (1989).
13. R. D. STAMBAUGH, H-mode Workshop Summary, Gut Ising, FRG (1989).
14. D. J. CAMPBELL, Private Communication (Nov. 1990).
15. R. E. WALTZ, *Bull. Am. Phys. Soc.* (1989).
16. H. BIGLARI et al., "Influence of Sheared $E \times B$ Rotation on Edge Turbulence Dynamics and Access to Enhanced Confinement Regimes," *Proc. 13th Int. Conf. Plasma Physics and Controlled Nuclear Fusion Research*, Washington, D.C., October 1-6, 1990, Vol. II, p. 191, International Atomic Energy Agency.
17. F. W. Perkins, Private Communication, 1991.
18. E. LAZZARO et al., "H-mode Confinement at Low q and High Beta in JET," *Nucl. Fusion*, **30**, 2157 (1990).

III.D. SPECIFIED PROFILE PERFORMANCE MODELING

D. P. Stotler (PPPL)

In this section, we discuss what are frequently called global, or zero-dimensional, characterizations of tokamak performance.¹⁻⁶ For this purpose, we have developed three approaches. They all investigate essentially the same power balance equation and likewise use the same plasma profile models and empirical scaling assumptions to compute the various terms in this equation.

Two of the approaches examine only the steady-state performance of a device. The first described below maps out the density-temperature operating space, given one set of the parameters required to complete the specification of the profiles and scaling assumptions. The result is a Plasma Operation CONtour (POPCON) plot.⁷ The second steady-state analysis takes into account the fact that we do not know with certainty the appropriate values of these plasma parameters. It allows us to specify instead a probability distribution for each of them, with the more certain ones receiving narrower distributions. Given these, it calculates a probability distribution for the level of performance of BPX.

The third analysis technique examines the time evolution of a discharge, given a complete set of plasma profile and scaling assumption parameters. Of course, more information is needed in this case to describe how the machine parameters vary in time. This analysis emulates the global plasma behavior computed by more sophisticated transport codes.^{8,9} Because of the lack of detail in the global simulations, they can be carried out very quickly, allowing many different scenarios to be examined in a short period of time.

We now describe the power balance equation and the assumptions used to evaluate the terms appearing in it. For this purpose, we consider only the POPCON analysis. Variations in the model incorporated into the other two codes are discussed in their respective subsections. Approaches such as the one presented here are properly referred to as "specified profile" in that the radial dependencies of the plasma density, temperature, and current density are specified on input rather than calculated.

The equation solved is

$$P_{\alpha} + P_{OH} + P_{aux} = P_{con} + P_{rad}. \quad (3.10)$$

The individual terms represent the volume-integrated contributions made to the total power balance by alpha, ohmic, and auxiliary heating; thermal conduction, $P_{con} \equiv W_{tot}/\tau_E$, and radiated losses are on the right side. At given values of the

volume-averaged electron density $\langle n_e \rangle$ and density-weighted, volume-averaged temperature $\langle nT \rangle / \langle n \rangle$, this expression is solved for P_{aux} , the auxiliary power required to maintain a steady state. Note that W_{tot} is the total thermal energy of the plasma, and τ_E is the global thermal energy confinement time. The latter is calculated as a function of the net input power $P_{in} \equiv P_\alpha + P_{OH} + P_{aux} - P_{rad}$.

In our model, P_{rad} is intended to refer to radiation processes that affect the core plasma power balance such as bremsstrahlung and synchrotron; we consider only the former here.³ The impact of edge impurity line radiation on confinement is, in effect, built into the empirical scalings for τ_E . By subtracting the centrally peaked radiation when computing P_{in} , we obtain the net power flowing into the "good confinement" zone between the core and the edge of the plasma. This practice is standard in zero-dimensional calculations³⁻⁶ and has some basis in more detailed simulations.¹⁰

In general, Eq. (3.10) must be solved numerically. More detail on the specific expressions for the various terms in Eq. (3.10) can be found in Refs. 5 and 6.

The following assumptions apply to all of the calculations discussed in this section. The device parameters are those appropriate to the BPX design: major radius $R = 2.59$ m, minor radius $a = 0.795$ m, triangularity $\delta = 0.35$, plasma current $I_p = 11.8$ MA, and toroidal magnetic field $B_T = 9$ T. The elongation of the separatrix flux surface should be 2.2. However, the present model utilizes concentric, elliptical flux surfaces of constant ellipticity. We equate this elongation with that of the 95% flux surface, $\kappa = 2$, obtained from two-dimensional equilibrium calculations.

For simplicity, the density profile as a function of radius r is written in the form

$$n(r) = n_0 \left(1 - \frac{r^2}{a^2} \right)^{\alpha_n}, \quad (3.11)$$

where $n_0 = \langle n \rangle (1 + \alpha_n)$. For the reference case (see Sec. III.C.6), $\alpha_n = 0.5$. The temperature profile is trapezoidal. Namely, it is flat from $r = 0$ to $r = r_{q=1}$ and falls linearly to $T = 0$ at $r = a$. We use $r_{q=1}/a = 1/q_{95} \simeq 0.29$ in the reference case [q_{95} is the magnetohydrodynamic (MHD) safety factor at the 95% flux surface]. The plasma is composed of deuterium and tritium (in equal amounts), as well as fully ionized carbon and helium impurities. Again, as discussed in Sec. III.C.6, we take the total effective charge of the plasma to be $Z_{eff} = 1.65$ and assume a helium fraction of $n_{He}/n_e = 3\%$.

The energy confinement time is written as

$$\tau_E = \min[\tau_{NA}, c_\tau \tau_{aux}(P_{in}, I_p, B_T, \dots)], \quad (3.12)$$

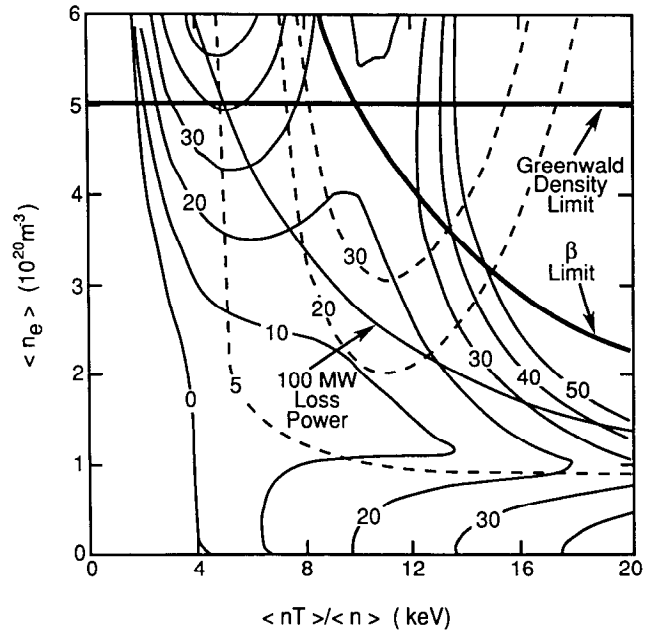


Fig. 3.16. POPCON of BPX operating space generated with 1.85 times the ITER89-P L-mode scaling. The solid lines are contours of constant auxiliary power in megawatts; the dashed lines are for Q . The Greenwald density limit, Troyon beta limit, and 100-MW loss power contour are also indicated.

where

$$\tau_{NA} = 7 \times 10^{-22} \bar{n}_e a R^2 q_* s \quad (3.13)$$

is the neo-Alcator (ohmic) contribution, with \bar{n}_e being the line-averaged electron density, and q_* is the cylindrical equivalent safety factor¹:

$$q_* = (5a^2 B_T / R I_p) \{ [1 + \kappa^2 (1 + 2\delta^2 - 1.2\delta^3)] \} / 2.$$

The second term in Eq. (3.12) represents one of a number of auxiliary heating scalings. The (constant) multiplier is included to estimate H-mode performance using L-mode scalings ($c_\tau \sim 2$) or to degrade H-mode scalings ($c_\tau \lesssim 1$).

III.D.1. POPCON Plots

We now compare POPCON plots generated using several different scalings for τ_E . The first (Fig. 3.16) represents the reference H-mode confinement model, which utilizes an auxiliary heating scaling of 1.85 times (see Sec. III.C) the ITER89-P L-mode scaling¹¹:

$$\tau_{aux}^{ITER89-P} = 0.0381 I_p^{0.85} B_T^{0.2} \bar{n}_e^{0.1} P_{in}^{-0.5} A_i^{0.5} R^{1.2} a^{0.3} \kappa^{0.5} s, \quad (3.14)$$

where $\bar{n}_{e,19}$ is the line-averaged density in units of 10^{19} m^{-3} , and \bar{A}_i is the average ion mass (taken here to be 2.5). This expression is inserted in Eq. (3.12) with $c_\tau = 1.85$. In addition to P_{aux} , contours of constant $Q \equiv P_{fus}/(P_{aux} + P_{OH}) = 5P_\alpha/(P_{aux} + P_{OH})$ are indicated.

Anticipated operating limits are also shown. The Greenwald form for the line-averaged density limit,

$$\bar{n}_{e,G} = \frac{I_p}{\pi a^2} \times 10^{20} \text{ m}^{-3}, \quad (3.15)$$

is used (note, however, that the ordinate of the POPCON diagram is the volume-averaged density). The Troyon beta limit is plotted assuming a coefficient of 3. Namely,

$$\beta_{max} = 3 \frac{I_p}{aB_T} \%. \quad (3.16)$$

The most stringent restriction is expected to be the limit on power flowing to the plasma edge (see Chaps. IX and X), projected to be limited to ≤ 100 MW; this is indicated by the 100-MW loss power ($P_{loss} \equiv P_\alpha + P_{OH} + P_{aux} = P_{con} + P_{rad}$) contour.

With this model, BPX is expected to reach $Q \simeq 25$ (see Fig. 3.16). The auxiliary power required at this operating point is slightly less than the 20 MW provided in the baseline configuration.

It would, of course, be more desirable to base our predictions on well-established scalings fitted to H-mode experiments directly. Expressions based on H-mode data are just now beginning to be developed, as has been discussed in Sec. III.C.3. In the following, we will compare POPCON plots generated using some of these with Fig. 3.16.

Specific experiments on DIII-D and JET have been performed to elucidate the scaling of H-mode confinement,¹² yielding

$$\tau_{aux}^{DSD-JET} = 0.0559 I_p^{1.03} P_{in}^{-0.46} \bar{A}_i^{0.5} R^{1.48} \kappa^{0.5} \text{ s}. \quad (3.17)$$

The resulting POPCON plot is presented in Fig. 3.17; the same operational limits are indicated. Note that the performance is slightly poorer than in Fig. 3.16; the maximum Q achievable is ~ 15 , depending on the amount of auxiliary power available.

Regression on the ITER H-mode data base has provided a number of scalings. Here we focus on two described in Ref. 13. The first expression is obtained by a direct fit to the standard data set (including shots with and without ELMs):

$$\tau_{aux}^{IH-SD} = 0.021 I_p^{0.55} B_T^{0.91} \bar{n}_{e,19}^{0.17} P_{in}^{-0.55} \bar{A}_i^{0.5} R^{2.11} a^{0.19} \kappa^{0.70} \text{ s}. \quad (3.18)$$

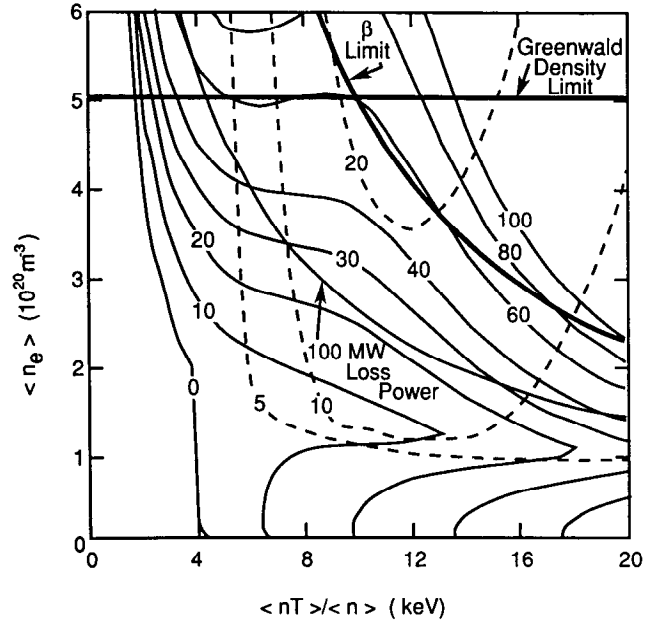


Fig. 3.17. POPCON of BPX operating space generated with the DIII-D/JET H-mode scaling.¹²

This yields the POPCON shown in Fig. 3.18. The appearance of a large ignited operating window (shaded region in Fig. 3.18) indicates more optimistic confinement than that of the standard scaling.

A more careful treatment of the ELM-free portion of the data base results in the ITER90H-P scaling¹³:

$$\tau_{aux}^{I90H-P} = 0.082 I_p^{1.02} B_T^{0.15} P_{in}^{-0.47} \bar{A}_i^{0.5} R^{1.60} \kappa^{-0.19} \text{ s}. \quad (3.19)$$

A POPCON plot generated using this expression is presented in Fig. 3.19. Again, a significant window for ignited operation is indicated. If we degrade this confinement by 20% to allow for ELMs (Ref. 14), we obtain a POPCON plot (Fig. 3.20) that is surprisingly similar to Fig. 3.16. ELMs may or may not naturally occur in BPX. It would be most interesting to study both ELMing and non-ELMing discharges.

We conclude from these POPCON plots that scalings obtained by direct fits to H-mode data predict BPX performance levels that are similar to those found using 1.85 times ITER89-P or more optimistic. Due to the complexity of the H-mode data base, however, the resulting scalings are somewhat uncertain, and at this time we do not use them as the basis for extrapolating to BPX parameters. Hence, in the following we focus on the more well-established ITER89-P scaling.

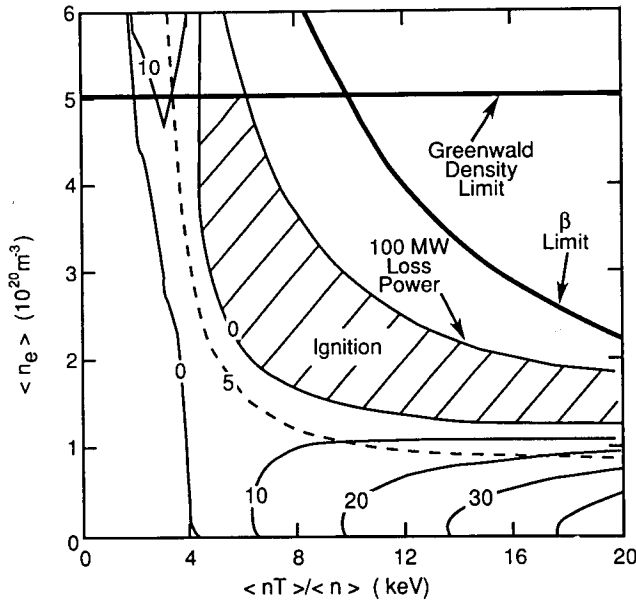


Fig. 3.18. POPCON of BPX operating space generated with the ITER H-mode "standard data set" scaling.¹³ Ignited operation is possible in the shaded region.

Variations in c_τ , α_n , and Z_{eff} within their estimated uncertainties can lead to substantial changes in predictions of BPX performance. We assume that each of these three parameters has a Gaussian distribution with its mean value as given above. The widths of these distributions are taken to be (see Sec. III.C.6) $\sigma_{c_\tau} = 25\%$, $\sigma_{\alpha_n} = 0.5$, and $\sigma_{Z_{eff}} = 0.35$. We now consider the impact of $\pm 1\sigma$ variations of each of these parameters on BPX performance.

The level of performance is expressed in terms of the maximum ignition margin obtainable within the constraints on $P_{loss} (\leq 100 \text{ MW})$ and the density, Eq. (3.15). The ignition margin is defined by

$$M_I = \frac{P_\alpha}{P_{con} + P_{rad}} \quad (3.20)$$

and is related to Q by

$$Q = \frac{5M_I}{1 - M_I}. \quad (3.21)$$

As can be seen from Eq. (3.10), ignited operation is indicated for $M_I \gtrsim 1$ ($Q \rightarrow \infty$). The procedure for carrying out this calculation is described elsewhere.^{6,15} The results are shown in Table 3.6 along with the ignition margin found using standard values for the three parameters.

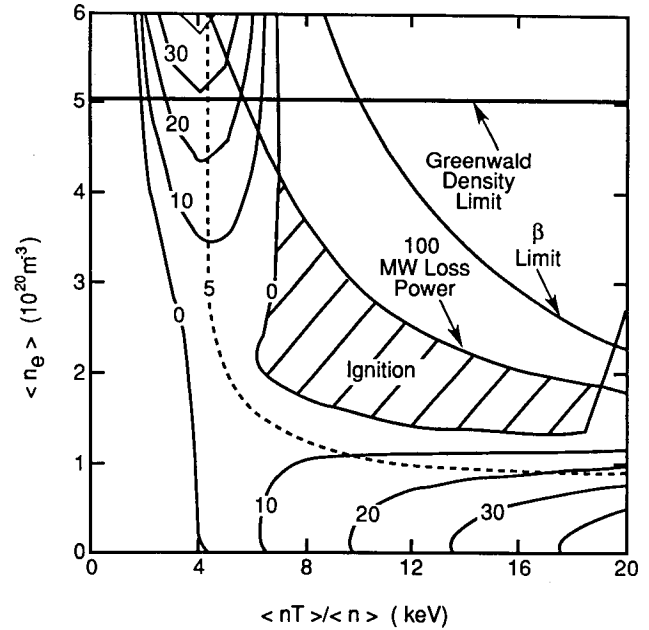


Fig. 3.19. POPCON of BPX operating space generated with the ITER90H-P scaling.¹³ Ignited operation is possible in the shaded region.

The Q determined with the mean values is 25, consistent with Fig. 3.16. Reducing the confinement multiplier by $1\sigma_{c_\tau}$ (but retaining the 3% helium concentration; see also Sec. III.D.2) lowers the performance estimate to $Q = 4.6$; the impact of reducing α_n or raising Z_{eff} is not so great. Going in the other direction, full ignition at $P_{loss} = 100 \text{ MW}$ is predicted for $c_\tau \geq 2.02$, less than $1\sigma_{c_\tau}$ above 1.85 ($c_\tau + 1\sigma = 2.31$). Optimistic assumptions for α_n and Z_{eff} with median confinement lead to subignited, but very high Q operating points.

III.D.2. Statistical Estimates of Performance Uncertainty

In the previous section, we considered varying c_τ , α_n , and Z_{eff} one at a time. If two or more of these were varied in the same direction at once, the effects would be greater than indicated in Table 3.6. It is not clear what single combination (if any) of parameters could be used to obtain a good measure of the uncertainty in performance. Instead, we use a Monte Carlo approach to generate a probability distribution for the ignition margin¹⁶ in BPX.

The procedure for doing this is described in more detail in Ref. 6. Briefly, one provides the code with probability distributions for c_τ , α_n , and Z_{eff} (and other parameters if desired). Then, a complete set of parameters is sampled randomly, and the maximum ignition margin is computed, subject to density and beta limits. The process is repeated until the statistical fluctuations in the resulting proba-

Table 3.6. Maximum Ignition Margin with $P_{loss} = 100$ MW

Case	c_τ	α_n	Z_{eff}	M_I	Q
Std.	1.85	0.5	1.65	0.8337	25.07
$c_\tau - 1\sigma$	1.39	0.5	1.65	0.4786	4.59
$\alpha_n - 1\sigma$	1.85	0.0	1.65	0.6868	10.97
$Z_{eff} + 1\sigma$	1.85	0.5	2.00	0.7146	12.52
$c_\tau + 1\sigma$	2.31	0.5	1.65	1.2219	∞
$\alpha_n + 1\sigma$	1.85	1.0	1.65	0.9702	162.95
$Z_{eff} - 1\sigma$	1.85	0.5	1.30	0.9593	117.97

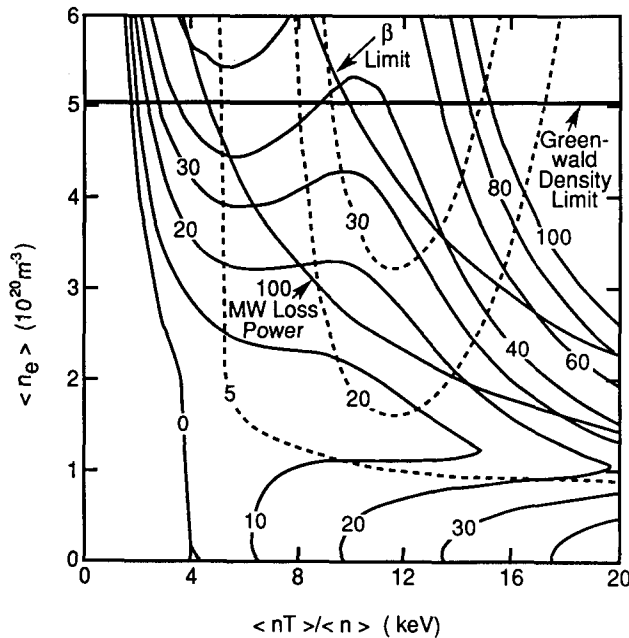


Fig. 3.20. POPCON of BPX operating space generated with the ITER90H-P scaling assuming a 20% degradation by ELMs.

bility distribution are insignificant (5000 trials in the following). The restriction on beta is set at $\beta \leq 2I_p/aB_T$ %, which corresponds approximately to $P_{fus} = 500$ MW.

Since $\alpha_n < 0$, $c_\tau < 0$ and $Z_{eff} < 1$ are not physically sensible, we must alter these distributions slightly. Randomly sampled parameters violating these restrictions are reset to the minimum values (we actually take the minimum $Z_{eff} = 1.2$). This leads to peaks in the resulting parameter probability distributions at the minimum values, although $c_\tau = 0$ is far enough away from the mean that this does not occur in practice. The mean values are altered from those given in the last section, but the medians are not. As we discuss below, it is the

median that we consider most interesting.

We also note that the lower values of Q (say, $\lesssim 25$) will likely be consistent with ash accumulations smaller than $n_{He}/n_e = 3\%$. In taking this into account, we make use of the fact that Q is most highly correlated with c_τ (see Refs. 6 and 16). Thus, we assume that n_{He}/n_e is a prescribed function of c_τ . The minimum is taken to be 1% (set by ICRF heating requirements; see Sec. VI.B.4); this applies when $c_\tau \leq 1.39$. The maximum of 3% is chosen if $c_\tau \geq 1.85$. Between these two values, the function varies linearly.

The resulting probability distribution for the ignition margin and its integral are shown in Fig. 3.21. The standard deviation, mean, and median of $P(M_I)$ are 0.4052, 0.9059, and 0.8556, respectively. The median (corresponds to $Q = 30$) is more representative of the average performance level since 50% of the cases calculated (with these input probability distributions) would do better than this; 50% would do worse. Regardless of how one attempts to define “+1 σ ” performance, ignition would be obtained. For the pessimistic direction, however, some care should be exercised since $P(M_I)$ is non-Gaussian. We utilize the fact that for a Gaussian distribution, approximately two-thirds of the values lie within one standard deviation of the mean. Hence, only $1/6 \approx 16\%$ of the points are more than 1σ below the mean. We take this to define the “-1 σ ” performance level. Counting 16% up from $M_I = 0$ in Fig. 3.21 yields $Q_{-1\sigma} = 5.45$. At $Q \approx 5.45$, setting $P_{fus} = 500$ MW corresponds to a higher-than-acceptable P_{loss} . Limiting P_{loss} to 100 MW, we obtain $Q = 4.6$.

A simple model for the scaling of M_I (and Q) with I_p for a range of BPX-like devices using ITER89-P scaling and fixed engineering and physics constraints ($B_T = 9$ T, $R/a = 3.24$, $R \propto I_p$), was developed. Using the above results to calibrate the model at $I_p = 11.8$ MA, we can extrapolate the median BPX performance and its

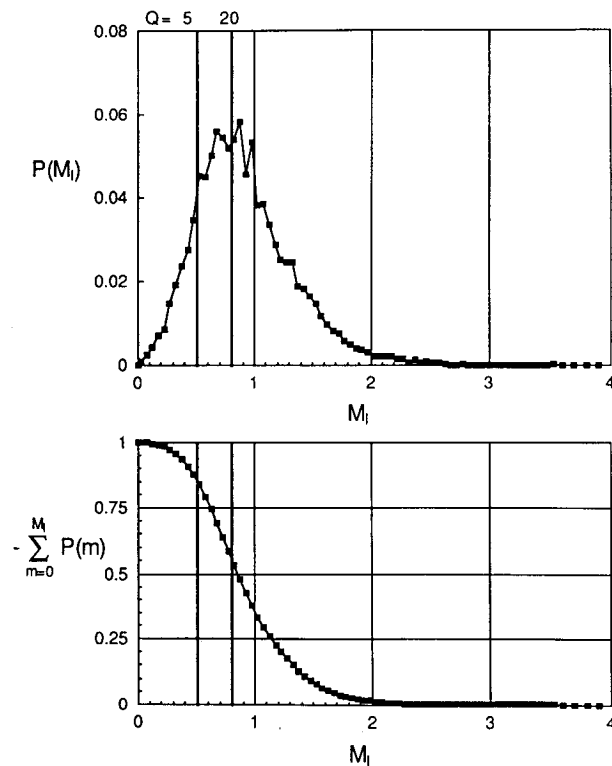


Fig. 3.21. Probability distribution of M_I and the integral of the probability distribution above a given M_I . The values of M_I corresponding to $Q = 5$ and 20 are indicated by vertical lines.

$\pm 1\sigma$ uncertainty to other values of the plasma current, as shown in Fig. 3.22.

To summarize the results of these two subsections, standard assumptions with 1.85 times the ITER89-P scaling yield $Q \sim 25$ to 30 . Pessimistic (at the 1σ level) values for these parameters lead to $Q \sim 5$. It may be worth noting that this analysis applied to the ITER Conceptual Design,¹⁷ with 10% helium minority, gives almost identical results to those presented here for BPX. The recent ITER H-mode scalings are more optimistic, giving rise to predictions of ignition for ELM-free operation in BPX.

III.D.3. Time-Dependent Simulations

We now consider the temporal evolution of BPX plasma parameters in several different situations. Our time-dependent global transport code employs the prescribed profile model and empirical scalings described in the introduction to this section.^{5,15} The scenarios we examine are based upon those

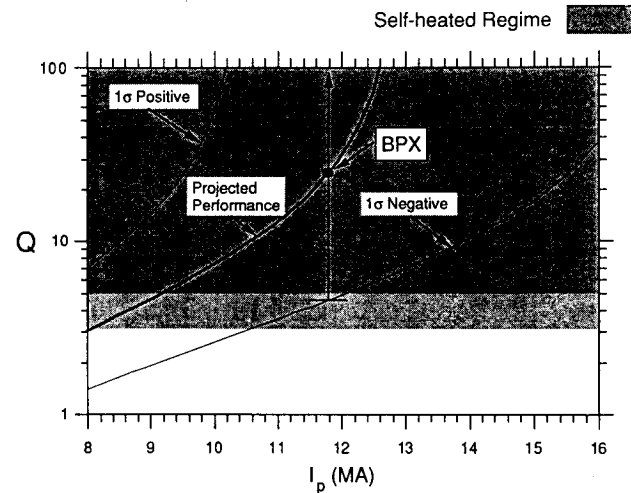


Fig. 3.22. Projected BPX performance range versus plasma current for fixed size. P_{loss} constrained to be ≤ 100 MW. Dark-shaded region indicates $Q > 5$.

produced by the more detailed Tokamak Simulation Code⁹ (TSC) (see Sec. V.G).

The equation being integrated is an adaptation of Eq. (3.10), modified to include the time derivative of the plasma energy:

$$\frac{dW_{tot}}{dt} = P_{\alpha} + P_{aux} + P_{OH} - P_{rad} - \frac{W_{tot}}{\tau_E}. \quad (3.22)$$

Given the initial conditions, the time dependence of the machine parameters, plasma density, and auxiliary power, Eq. (3.22) can be integrated to some final time t_f to determine $W_{tot}(t_f)$. We provide a mechanism for feedback on the auxiliary power level to prevent a specified value of P_{loss} from being exceeded.^{5,15} For most of the simulations presented here, we require $P_{loss} \leq 100$ MW, as specified in the BPX General Requirements Document¹⁸ (GRD).

The time dependence of the device parameters (Fig. 3.23) is based upon the ones used in the TSC calculations. For simplicity, the simulations begin at $t = 1.5$ s. The flattop parameters needed to compute the right side of Eq. (3.22) are as in Sec. III.D, except where noted below. We employ two scenarios for the evolution of P_{aux} and the plasma density, but in all cases the maximum value of P_{aux} will be set to 20 MW, as specified in the baseline BPX design. The first operating scheme (referred to hereafter as scenario I) is patterned after the default waveforms in TSC and has the density ramping up linearly to its flattop value with the plasma current (Fig. 3.24a) at $t = 7.5$ s. Auxiliary heating is begun at $t = 5$ s. Its efficiency is approximated as being equal to the value

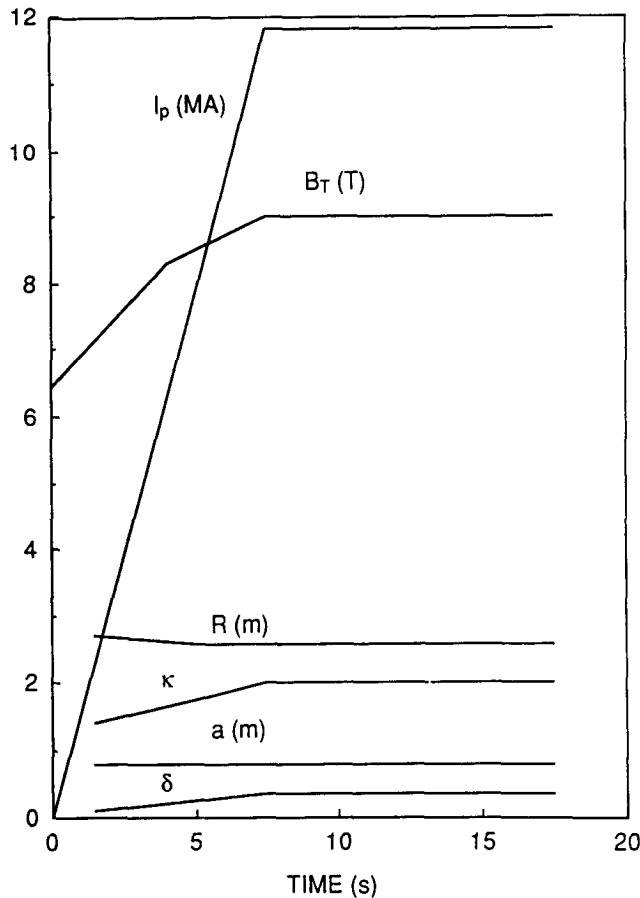


Fig. 3.23. Evolution of BPX parameters in the time-dependent global transport code. Units for each quantity are shown in parentheses. The flat-top ends at $t = 17.5$ s; rampdowns are not shown.

of the density at the ion cyclotron resonance point, divided by the central density.^{15,19}

Since power handling capabilities limit burn times to values shorter than the total BPX flat-top (see below, as well as Chaps. IX and X), we have as an option delaying the start of auxiliary heating until after the plasma current has reached its maximum value. In this way, the thermal confinement is nearly optimal when heating begins. In the second scenario (see Fig. 3.24b), we make use of this fact; heating begins at $t = 8$ s. The density is ramped linearly up to half of its peak value during the current rise. Since the early portion of an H-mode discharge (the transition is assumed to occur soon after the activation of auxiliary power) usually exhibits an increase in density, we incorporate a second density ramp beginning at $t = 8$ s. We will be providing significant fueling with pellet injection, so we allow ourselves to vary the rate of this density rise, choosing the value that minimizes

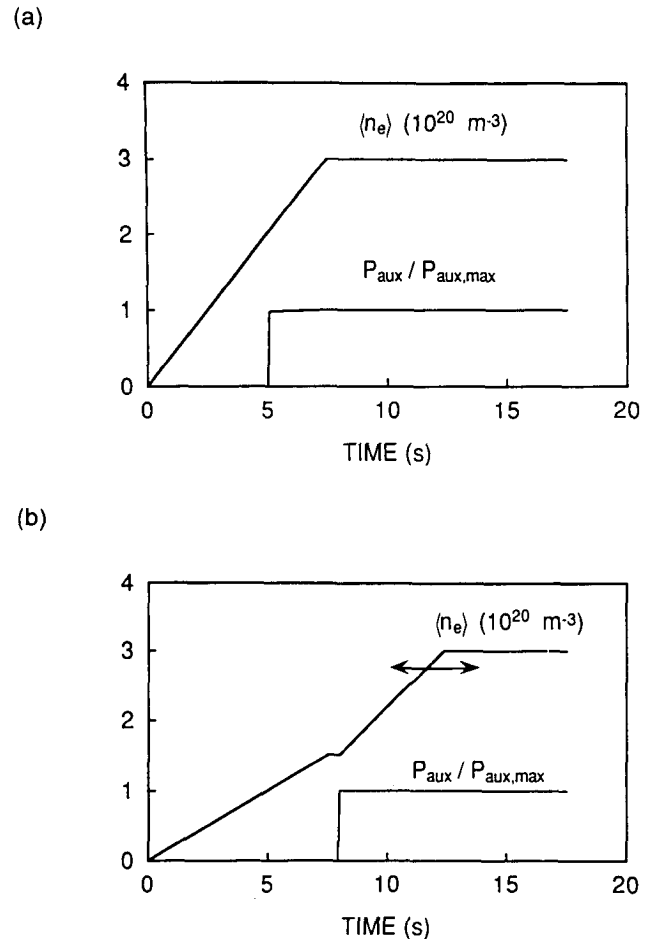


Fig. 3.24. Time dependence of the plasma density and heating efficiency for scenarios I (a) and II (b). The actual flat-top density is varied to yield the desired final operating point. The arrow on density waveform in scenario II indicates the optimization of the second ramp rate in order to minimize the heating time.

the total heating time.

We use an expression for the energy confinement time in which the input power has been eliminated in favor of purely thermodynamic quantities. Although this approach yields more optimistic results than does using the form of τ_E expressed in terms of heating power, it is more consistent with the conjecture that transport is determined by local plasma parameters. It is also consistent with the definition of τ_E used in the H-mode data base:

$$\tau_E \equiv W_{tot} / \left(P_{in} - \frac{dW_{tot}}{dt} \right).$$

The procedure for making this conversion in the form of τ_E and its impact on time-dependent calculations are discussed in detail in Ref. 5.

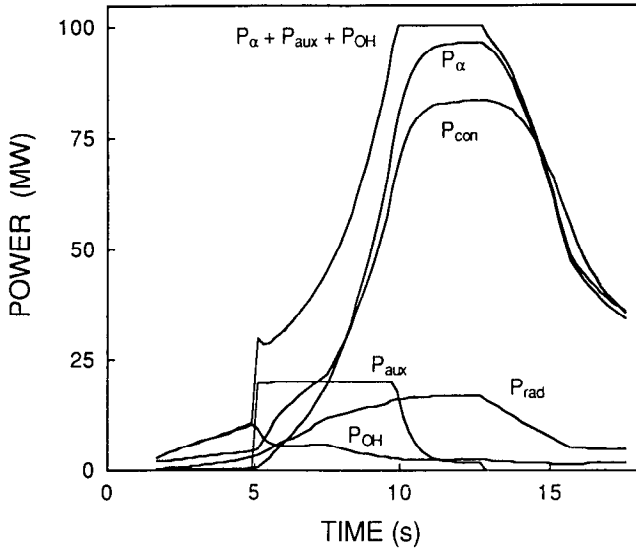


Fig. 3.25. Time dependence of the various terms in Eq. (3.22) and $P_{loss} = P_{\alpha} + P_{aux} + P_{OH}$. The density and auxiliary power are specified by scenario I. All parameters have their reference values, except the confinement multiplier, which is assumed to be slightly optimistic ($c_{\tau} = 2$).

All of these calculations utilize a constant Z_{eff} of 1.65, and all assume a steady helium ash concentration of 3% unless otherwise stated.

Before presenting the detailed results of our simulations, it would be appropriate to discuss how they relate to one another and to the reference BPX operating scenario. At $P_{loss} = 100$ MW ($P_{fus} \lesssim 500$ MW), we are at a “center-of-the-error-bars” level of performance for the device, both with respect to confinement and power handling capability. The restrictions on the total energy flowing out of the plasma are discussed in more detail in the GRD. For present purposes, we estimate the power handling capability of the divertor at:

$$\int_{t_1}^{t_2} P_{loss} dt \leq 625 \text{ MJ}, \quad (3.23)$$

where $t_1 \equiv 5$ s is intended to represent the time at which the plasma first touches the divertor, and t_2 is one second into the rampdown of P_{loss} . The latter choice assumes a switch from a divertor to limiter configuration at t_2 .

With 20 MW of auxiliary heating, Eq. (3.23) can be satisfied with the 3-s flattop at $P_{loss} = 100$ MW specified in the GRD, provided the plasma performance is slightly better than that of the reference case ($c_{\tau} \sim 2$). The simulation presented in Fig. 3.25 provides an example of this. With the reference level of plasma performance, the $P_{loss} = 100$ MW flattop can be achieved with $P_{aux} = 20$ MW,

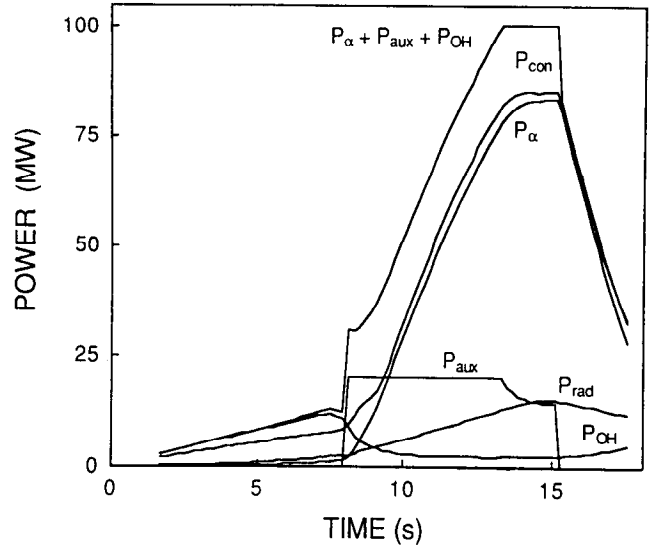


Fig. 3.26. Time dependence of the various terms in Eq. (3.22) and $P_{loss} = P_{\alpha} + P_{aux} + P_{OH}$. The density and auxiliary power are specified by scenario II. All parameters have their standard values.

but some of the power handling capability of the divertor is used during the rampup, and the flattop must be less than 3 s. ($\tau_{ft} \sim 2$ s) if Eq. (3.23) is to be satisfied. This mode of operation is demonstrated in Fig. 3.26. On the other hand, still assuming reference plasma performance, a 3-s flattop can be retained if the flattop value of P_{loss} is held below 100 MW ($P_{loss} = 87$ MW). This might be accomplished by reducing the plasma density; this approach is considered in Fig. 3.27.

As can be seen, the full 3-s flattop cannot be achieved with the precise “center-of-the-error-bars” confinement and divertor performance. However, it is also clear that this point is somewhat singular: Slightly higher confinement gives the full flattop because the heating phase is reduced in length; lower confinement also gives an adequate flattop because the maximum output power is reduced, as is shown in the extreme example of $Q = 5$ in Fig. 3.28. The BPX device and facility are designed to accommodate a heating power upgrade to as high as 50 MW. This is more than adequate for present purposes in that only 26 MW of external heating would be required, for example, to speed the rampup shown in Fig. 3.26 sufficiently to allow the full flattop to be attained while still satisfying Eq. (3.23).

For the simulation in Fig. 3.25, we use scenario I (Fig. 3.24a) and $c_{\tau} = 2$ (less than 0.4 standard deviations above the reference value). The final operating point obtained in a steady-state analysis¹⁵ is at $\langle n_e \rangle = 2.9 \times 10^{20} \text{ m}^{-3}$, $\langle nT \rangle / \langle n \rangle = 10$ keV with $P_{\alpha} = 96$ MW, $P_{rad} = 17$ MW, and $P_{aux} = 1.5$

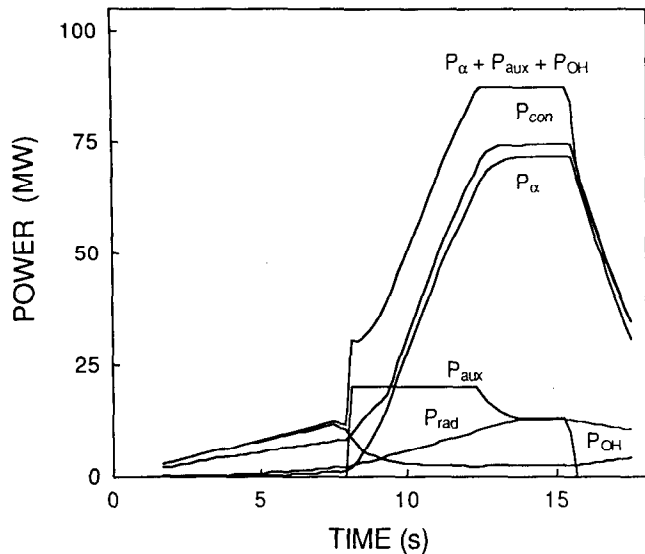


Fig. 3.27. Time dependence of the various terms in Eq. (3.22) and $P_{loss} = P_{\alpha} + P_{aux} + P_{OH}$. The density and auxiliary power are specified by scenario II. The peak value of $P_{loss} = 87$ MW. All parameters have their standard values.

MW. It is reached at $t = 11.7$ s, about two seconds after the feedback circuit begins enforcing $P_{loss} \leq 100$ MW. The rampdown (consisting of setting $P_{aux} = 0$) starts at $t = 12.9$ s. In addition, the density is ramped down to half of its maximum value in three seconds; this is necessary in order to hasten the P_{loss} falloff. Operationally, it is planned to move the plasma to the inner wall, where density pump-out can be hastened and the H-mode may be quenched. If necessary, impurity injection can be used as well. The current rampdown phase is discussed in more detail in Chap. V.

In Fig. 3.26, we utilize scenario II (Fig. 3.24b) and reference performance parameters. The final state is $\langle n_e \rangle = 2.7 \times 10^{20} \text{ m}^{-3}$, $\langle nT \rangle / \langle n \rangle = 10$ keV with $P_{\alpha} = 83$ MW, $P_{rad} = 15$ MW, and $P_{aux} = 14$ MW. The $P_{loss} = 100$ MW flattop begins at $t = 13.3$ s; approximately one second later, the operating point is reached. In order to satisfy Eq. (3.23), the length of the flattop must be shortened to 1.9 s. Because Q is somewhat lower here than in scenario 1, no reduction in density is required during the rampdown. Any density pump-out that can be provided will serve only to bring down P_{loss} more quickly.

The simulation in Fig. 3.27 is virtually the same as that in Fig. 3.26, except that the density has been reduced to $\langle n_e \rangle = 2.5 \times 10^{20} \text{ m}^{-3}$ and the flattop value of P_{loss} has been set to 87 MW. Other parameters describing this operating point are $\langle nT \rangle / \langle n \rangle = 10$ keV, $P_{\alpha} = 72$ MW, $P_{rad} = 13$ MW, and $P_{aux} = 13$ MW; $Q = 23$ in this case. The

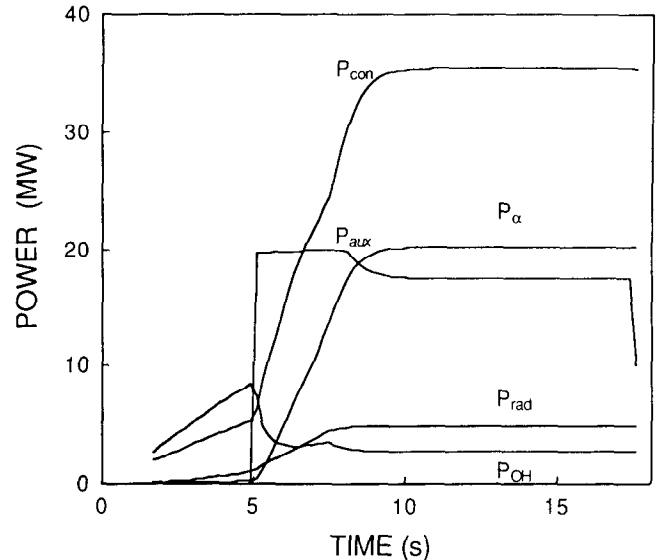


Fig. 3.28. Time dependence of the various terms in Eq. (3.22) and $P_{loss} = P_{\alpha} + P_{aux} + P_{OH}$. The density and auxiliary power are specified by scenario I. This is a minimum performance case with $c_{\tau} = 1.6$, $\alpha_n = 0.2$, $Z_{eff} = 1.9$, and $n_{He}/n_e = 1.0\%$.

P_{loss} flattop and the operating point are attained earlier in the discharge ($t = 12.5$ s and $t = 13.7$ s, respectively) than in Fig. 3.26. This is a result of the lower thermal energy of the operating point and the extra 1 MW obtained from the lower steady-state P_{aux} . Because of this more rapid heating and the reduced limit on P_{loss} , a full 3-s flattop can be carried out without violating Eq. (3.23).

Finally, we consider a low-performance case. Namely, we assume $c_{\tau} = 1.6$, $\alpha_n = 0.2$, and $Z_{eff} = 1.9$; correspondingly, we take a lower ash concentration ($n_{He}/n_e = 1.0\%$). The final operating point is $\langle n_e \rangle = 1.6 \times 10^{20} \text{ m}^{-3}$, $\langle nT \rangle / \langle n \rangle = 9.0$ keV with $P_{\alpha} = 20$ MW, $P_{rad} = 4.9$ MW, and $P_{aux} = 17$ MW. We arbitrarily set the maximum value of P_{loss} at 40 MW, as shown in Fig. 3.28. Because this is so far below the 100 MW that represents the upper end of the BPX operating range, the P_{loss} flattop is limited only by the plasma current pulse length.

REFERENCES

1. N. A. UCKAN and J. SHEFFIELD, "A Simple Procedure for Establishing Ignition Conditions in Tokamaks," *Tokamak Startup*, p. 45, H. KNOEPFEL, Ed., Plenum Press, New York (1986).
2. O. MITARAI, A. HIROSE, and H.M. SKARSGARD, "Generalized Ignition Contour Map and Scaling Law Requirement for Reaching Ignition in a Tokamak Reactor," *Nucl. Fusion*, **28**, 2141 (1988).

3. N. A. UCKAN, "Relative Merits of Size, Field, and Current on Ignited Tokamak Performance," *Fusion Technol.*, **14**, 299 (1988).
4. R. E. WALTZ, R. R. DOMINGUEZ, and F. W. PERKINS, "Drift Wave Model Tokamak Ignition Projections with a Zero-Dimensional Transport Code," *Nucl. Fusion*, **29**, 351 (1989).
5. D. P. STOTLER and N. POMPHREY, "Pulse Length Assessment of Compact Ignition Tokamak Designs," *Fusion Technol.*, **17**, 577 (1990).
6. D. P. STOTLER, R. J. GOLDSTON, and the CIT Team, "Ignition Probabilities for Compact Ignition Tokamak Designs," PPPL-2629, Princeton Plasma Physics Laboratory (1989); and *Fusion Technol.* **20**, 7 (1991).
7. W. A. HOULBERG, S. E. ATTENBERGER, and L. M. HIVELY, "Contour Analysis of Fusion Reactor Plasma Performance," *Nucl. Fusion*, **22**, 935 (1982).
8. C. E. SINGER et al. *Comput. Physics Commun.*, **49**, 275 (1988).
9. S. C. JARDIN, N. POMPHREY, and J. DE LUCIA, "Dynamic Modeling of Transport and Positional Control of Tokamaks," *J. Comput. Phys.*, **66**, 481 (1986).
10. M. H. REDI, W. M. TANG, P. C. EFTHIMION, D. R. MIKKELSEN, and G. L. SCHMIDT, "Transport Simulations of Ohmic TFTR Experiments with Microinstability Based, Profile Consistent Models for Electron and Ion Thermal Transport," *Nucl. Fusion*, **27**, 2001 (1987).
11. P. N. YUSHMANOV, T. TAKIZUKA, K. S. RIEDEL, O. J. W. F. KARDAUN, J. G. CORDEY, S. M. KAYE, and D. E. POST, "Scalings for Tokamak Energy Confinement," *Fusion Technol.*, **30**, 1999 (1990).
12. D. P. SCHISSEL, J. C. DeBOO, K. H. BURRELL, J. R. FERRON, R. J. GROEBNER, H. St. JOHN, R. D. STAMBAUGH, B. J. D. TUBBING, K. THOMSEN, J. G. CORDEY, M. KEILHACKER, D. STORK, P. E. STOTT, and A. TANGA, "H-Mode Energy Confinement Scaling From the DIII-D and JET Tokamaks," *Nucl. Fusion*, **31**, 73 (1991).
13. "Regression on Global Plasma Parameters," ITER (1990).
14. D. E. POST and the ITER Team, "ITER: Physics Basis," *Proc. 13th Int. Conf. Plasma Physics and Controlled Nuclear Fusion*, Washington, DC, October 1-6, 1990, paper IAEA-CN-53/F-1-3, International Atomic Energy Agency.
15. D. P. STOTLER, W. T. REIERSEN, and G. BATEMAN, "Systems Code Physics Package Documentation," Princeton Plasma Physics Laboratory Report (to be written).
16. S. K. HO and L. J. PERKINS, "Probability of Ignition: A Better Approach than Ignition Margin," *Nucl. Fusion*, **29**, 81 (1989).
17. ITER Team, "ITER Concept Definition," Vol. 1, International Atomic Energy Agency (1989).
18. "BPX General Requirements Document," Princeton Plasma Physics Laboratory.
19. P. COLESTOCK, Princeton Plasma Physics Laboratory, Private Communication (1990).